Interstellar and Ejecta Dust in the Cas A Supernova Remnant

Richard G. Arendt[1,2], Eli Dwek[2], Gladys Kober[2,3], Jeonghee Rho[4,5], and Una Hwang[6,7]

ABSTRACT

The ejecta of the Cas A supernova remnant has a complex morphology, consisting of dense fast-moving line emitting knots and diffuse X-ray emitting regions that have encountered the reverse shock, as well as more slowly expanding, unshocked regions of the ejecta. Using the *Spitzer* 5–35 μm IRS data cube, and *Herschel* 70, 100, and 160 μm PACS data, we decompose the infrared emission from the remnant into distinct spectral components associated with the different regions of the ejecta. Such decomposition allows the association of different dust species with ejecta layers that underwent distinct nuclear burning histories, and determination of the dust heating mechanisms. Our decomposition identified three characteristic dust spectra. The first, most luminous one, exhibits strong emission features at ~ 9 and 21 μm, and a weaker 12 μm feature, and is closely associated with the ejecta knots that have strong [Ar II] 6.99 μm and [Ar III] 8.99 μm emission lines. The dust features can be reproduced by magnesium silicate grains with relatively low MgO-to-SiO$_2$ ratios. A second, very different dust spectrum that has no indication of any silicate features, is best fit by Al$_2$O$_3$ dust and is found in association with ejecta having strong [Ne II] 12.8 μm and [Ne III] 15.6 μm emission lines. A third characteristic dust spectrum shows features that best matched by magnesium silicates with relatively high MgO-to-SiO$_2$ ratio. This dust is primarily associated with the X-ray emitting shocked ejecta and the shocked interstellar/circumstellar material. All three spectral components include an additional featureless cold dust component of unknown composition. Colder dust of indeterminate composition is associated with [Si II] 34.8 μm emission from the interior of the SNR, where the reverse shock has not yet swept up and heated the ejecta. The dust mass giving rise to the warm dust component is about ~ 0.1 M$_\odot$. However, most of the dust mass is associated with the unidentified cold dust component. Its mass could be anywhere between 0.1 and 1 M$_\odot$,

---

[1] CRESST, University of Maryland – Baltimore County, Baltimore, MD 21250, USA; Richard.G.Arendt@nasa.gov

[2] NASA Goddard Space Flight Center, Code 665, Greenbelt, MD 20771, USA

[3] Department of Physics, IACS, Catholic University of America, Washington DC 20064, USA

[4] SETI Institute, 189 Bernardo Ave, Mountain View, CA 94043

[5] SOFIA Science Center, NASA Ames Research Center, MS 211-3, Moffett Field, CA 94035

[6] NASA Goddard Space Flight Center, Code 662, Greenbelt, MD 20771, USA

[7] The Henry A. Rowland Department of Physics and Astronomy, Johns Hopkins University, 3400 N. Charles Street, Baltimore, MD 21218, USA

and is primarily limited by the mass of refractory elements in the ejecta. Given the large uncertainty in the dust mass, the question of whether supernovae can produce enough dust to account for ISM dust masses in the local and high-z universe remains largely unresolved.

Subject headings: dust, extinction — infrared: ISM — ISM: individual (Cassiopeia A) — supernova remnants

1. INTRODUCTION

Interstellar dust models that fit the average interstellar extinction curve, the diffuse infrared emission and scattering, and abundances constraints (Li & Draine 2001; Zubko, Dwek, & Arendt 2004; Brandt & Draine 2012) employ a very limited variety of dust compositions, consisting primarily of polycyclic aromatic hydrocarbons (PAHs), graphite or amorphous carbon, and astronomical silicates. Yet observations of specific interstellar dust sources, meteoritic inclusions, and interplanetary dust particles (IDPs) reveal a significantly richer variety of dust compositions. Examples are magnesium sulfides (MgS) found in the atmospheres of AGB stars near the Galactic Center (Chan et al. 1997), and presolar grains of SN or stellar origin, such as silicate carbide (SiC), silicon nitride (Si_3N_4), and aluminum, calcium- and titanium-oxides (e.g. Zinner 2008). Their absence in interstellar dust models suggests that they are not required for fitting the various manifestation of dust in the general ISM, either because of their low abundance relative to silicates and carbonaceous dust, or due to the fact that they may have been processed in the ISM.

Supernovae can be important sources of interstellar dust. They produce all the refractory elements needed for the formation of dust, and their ejecta largely retain the compositional inhomeogeneity of the progenitor star. They may therefore be sources of dust with unusual chemical compositions. Furthermore, SN are the drivers of the chemical evolution in galaxies, and therefore potentially the most important sources of interstellar dust. In fact, SN are the *only* source of newly condensed dust in high redshift galaxies, before low mass stars evolved off the main sequence. Determining the mass and composition of SN condensed dust is therefore key for understanding the origin, evolution, and processing of dust in galaxies.

The Cas A remnant is an ideal object for studying the composition and abundance of dust that formed in the ejecta of core collapse SNe. The SN was not definitively recorded at the time that it occurred. Studies of the expansion of the SNR estimate that the explosion was in the year 1681±19 (Fesen et al. 2006). Yet fortunately, light echoes of the Cas A SN have allowed studies of this old event with modern instruments. Such observations have revealed that Cas A was a Type IIb SN (Krause et al. 2008) with distinct asymmetry in its explosion (Rest et al. 2011). Dynamical and compositional asymmetries are still imprinted on the Cas A SNR today, but the dominant structure of the Cas A SNR is characterized by a clear distinction between the forward shock sweeping up the interstellar (and/or circumstellar medium) and the reverse shock through which the SN ejecta is expanding.

The ejecta consists of three main components: the first, containing most of the mass, consists of a low density phase that is heated by the reverse shock to X-ray emitting temperatures ($\gtrsim 10^6$ K). The second component consists of dense fast-moving knots (FMKs) that have gone through the reverse shock, and are radiatively cooling by line emission at optical and IR wavelengths. A third component comprises ejecta that has not yet encountered the reverse shock, and is primarily heated by the ambient radiation within the SNR interior.

In this paper we revisit the analysis of the mid-IR spectra of the dust in Cas A. The infrared emission arises from dust residing in the circumstellar/interstellar (CS/IS) medium that is shocked by the advancing SN blast wave, from dust in the diffuse X-ray emitting and dense line emitting knots that encountered the reverse shock, and from dust in yet unshocked regions of the ejecta. Our main goal is to decompose the IR emission into its different spatial components in order to determine the mass, composition, and the specific regions of the ejecta in which the dust was formed. Our approach will therefore provide important information on the physical processes that facilitate or inhibit the nucleation of dust in the different layers of the ejecta, the resulting dust composition, and the dust heating mechanisms that give rise to the IR emission. Our approach is significantly different from previous ones (Ennis et al. 2006; Rho et al. 2008) which only grouped the IR emission into distinct spectral components, with no relation to the nature of the ejecta from which they originated.

To decompose the IR spectrum into the different components of the ejecta, we use multi wavelength observations of the remnant as proxies for their composition and spatial distribution. We use the radio synchrotron emission to represent the shocked CS/IS medium, the *Chandra* X-rays emission to represent the shocked diffuse ejecta, and the *Spitzer* fine-structure IR emission lines to represent the dense FMK. The description of the data sets used in the analysis and the construction of the different spectral templates representing the different components of the ejecta are described in §2. In §3 we describe the decomposition of the dust into the different spectral templates, and derive the IR spectra associated with each template. In §4 we derive the minimal dust mass and composition required to fit the IR emission associated with each template. The discussion in §5 assembles the results to create a clearer picture of just what can and cannot be constrained from the analysis of the mid-IR emission of Cas A. The overall results of the paper are summarized in §6.

2. DEFINING THE SPECTRAL/SPATIAL TEMPLATES OF THE EJECTA

2.1. Data Preparation

Work began with the low resolution IRS spectral data cubes used by Rho et al. (2008). There are 4 cubes, generated from the 1st and 2nd order spectra in short and long wavelength low resolution modules. At each wavelength, the data were convolved to the resolution at the longest IRS wavelength, 38.33 μm, using kernels derived from Tiny Tim/ Spitzer (STINYTIM)[7] PSFs according to Gordon et al. (2008). The three shorter wavelength cubes were then reprojected to the same scale and orientation as the longest wavelength (SL1) cube. The data are then combined into a single IRS low-resolution cube covering 5 - 38 μm with a fixed spatial resolution. Weighted averages were used at the wavelengths that overlap between the different spectral orders and modules.

For the purpose of analyzing the dust emission, we created a continuum spectral cube by replacing all the emission lines with a smooth polynomial fit to the continuum on either side of each line. This procedure is performed independently for each spatial pixel of the cube and each line. It avoids any need to fit the lines themselves, which can be found at various velocity components at each pixel because of the high expansion velocities of Cas A. The lines that were thus removed are listed in the row and column headings of Table 1. Finally, to remove remaining artifacts and improve the signal to noise, the continuum cube was smoothed in wavelength to a spectral resolution of $R = \lambda/\Delta\lambda \approx 20$, and trimmed to a maximum wavelength of 35 μm.

Longer wavelength information was obtained by using Herschel PACS observations at 70, 100, and 160 μm, with the appropriate spatial convolution of the 70 and 100 μm images whose native resolution is better than the IRS at 38 μm. At 160 μm the SNR is substantially confused by ISM emission. This confusion was reduced by subtracting an empirically scaled version of the SPIRE 250 μm image in which the synchrotron emission of the SNR was subtracted by extrapolation from the 350 and 500 μm bands. The subtraction is an improvement, but is still imperfect, in part due to the lower spatial resolution of the longer wavelength SPIRE data.

The synchrotron emission is removed from the final *Spitzer+Herschel* continuum cube by subtraction of the VLA radio template (below) extrapolated assuming a power law spectrum $S_\nu \sim \nu^{-0.71}$.

2.2. Spatial Templates

A set of templates are needed to identify the spatial distribution of various physical components of the ejecta. The primary source for templates are the line emission maps that are generated by subtracting the continuum cube from the full data cube, and then integrating over the [-6000,+8000] km s^{-1} velocity range for each of the emission lines in the IRS spectrum. Most of these lines are associated with the fast-moving knots of ejecta. These knots tend to be O-rich, but there are some variations in composition that tend to be correlated with spatial and kinematic differences. Because of the large velocity range in Cas A, we did not disentangle the closely spaced [O IV] 25.89 μm and [Fe II] 25.99 μm lines.

---

[7] http://irsa.ipac.caltech.edu/data/SPITZER/docs/dataanalysistools/tools/contributed/general/stinytim/

Several other spatial templates were also tested. These are intended to trace the presence of dust in a wider range of environments than the relatively cool and dense line-emitting knots. (1) A radio template was derived from 6 cm VLA image of Cas A (DeLaney 2004). The region of the forward shock is traced more clearly in the radio than at most other wavelengths, and the bright radio knots in the reverse shock region are a different population than line-emitting ejecta knots. (2) and (3) X-ray Fe and Si templates were derived from *Chandra* observations (Hwang et al. ????), integrated over the widths of the 6.4 keV Fe and 1.7 keV Si K α lines. The X-ray continuum is included in these integrations. These templates trace ejecta in regions of lower density and much higher temperature. This include the bulk of the mass of the ejecta of the SN. (4) the IRAC 4.5 μm image lies outside the range of the IRS spectral coverage and contains both a line emission component and a synchrotron component. The synchrotron emission was subtracted using a scaled version of the IRAC 3.6 μm image which is dominated by synchrotron emission and has only weak line emission. This also over-subtracts stellar sources in the image. Thus regions where negative values resulted were replaced by nearby background values. (5) The IRAC 8 μm image is dominated by the [Ar II] 6.99 μm emission, but could potentially be a more sensitive tracer of this emission than the IRS line maps. The background ISM emission at 8 μm was removed by subtracting a scaled version of the 5.8 μm IRAC image, where the SNR emission is relatively weaker. As with the 4.5 μm template, the over-subtracted stellar sources were replaced by the local background levels. Each of these templates is convolved and reprojected to match the IRS continuum data cube.

This full set of templates would be expected to contain some degeneracies, where different lines (especially from the same species or element) would be tracing the same physical component of the SNR. To select a useful subset of the possible templates, we calculated the linear correlation coefficient for each pair of templates. These are listed in Table 1. The table shows which templates are well-correlated with others. Based on these correlations we sorted the templates in to similar groups and selected one template to represent each group. Images of the selected templates are shown in Figure 1.

There are several points of interest in the correlations listed in Table 1. Even though the [Ar II] and [Ar III] emission are very well correlated (as expected), we chose to keep both these templates in order to monitor for changes in the dust that might be related to the ionization state of the gas. It was not expected that highly ionized species such as [S IV] would correlate so well with [Ar II]. This correlation may become significantly weaker if higher spatial resolution data were available. Correlations involving the [Fe II] line are weaker than most due to the low signal to noise ratio of this line. The [Ne V] line is also relatively weak, yet surprisingly it correlates better with the [Ar II] group than the [Ne II] and [Ne III] lines. Despite an absence of Ne lines in the band, the 4.5 μm IRAC μm emission is somewhat better correlated with the Ne group templates than the Ar group. In particular, the “Ne crescents” noted by Ennis et al. (2006) are present in the IRAC 4.5 μm image. Although the [S III] 33.48 μm correlates moderately well with the [S III] 18.71 μm line, it does not correlate as well with the other templates of Ar group. This is an indication of variation in the S III line ratios, which would indicate large scale variations in the density of the ejecta. The [O IV]+[Fe II] template is distinct from the others, but we did not use it because as a blend of two lines it is likely to represent a mixture of different dust types and environments. The X-ray Si template is in fact distinct from the X-ray Fe template, but it was not used because initial analysis using only the X-ray Fe template did not indicate the presence of any residual emission that would have been compensated for by the addition of an X-ray Si template.

3. DERIVING THE INFRARED SPECTRA OF THE DIFFERENT TEMPLATES

3.1. Characteristic Template Spectra

One of the primary goals of this analysis was to find the continuum spectra that are associated with zones of various physical parameters and compositions throughout the SNR. To identify the spectra associated with each of the six emission templates shown in Fig. 1, we superimposed all the templates and for each one we identified the zones where its relative emission was the dominant component. Because of the strong and widespread [Ar II] emission, in some case the zones necessarily included a significant [Ar II] emission as well. The zones selected for each of the templates are outlined in Figure 2.

For the selected pixels, i, of each zone, we performed a linear fit to the spectra, $D(i,\lambda)$:

$$D(i,\lambda) = \sum_{j=1}^{6} S_j(\lambda) T_j(i) \; + \; C(\lambda) \tag{1}$$

where $T_j(i)$ are the 6 selected emission templates. The derived parameters are $C(\lambda)$, a constant term (which should be small) to account for errors in the background levels, and $S_j(\lambda)$, the spectra of each of the emission components. The characteristic spectra derived are shown in Figure 3.

When these derived spectra are multiplied by the spatial templates over the entire SNR (not just the selected zones where each was derived) and the resulting model is subtracted from the data cube, we found that there was one region of particularly strong residual emission, consistently positive at all wavelengths. This region is in the south central portion of the SNR. One additional zone was created to cover this region (the "South Spot" in Fig. 2), and the spectrum extracted from this zone is shown in Fig. 3.

3.2. Spatial Distribution of the Characteristic Spectra

The final step in the decomposition of the continuum spectral cube is to repeat the sort fitting given by Equation (1), but this time we use the seven $S_k(\lambda)$ spectra as known quantities, and solve for the spatial distributions of each component over the entire SNR.

$$D(i,\lambda) = \sum_{k=1}^{7} S_k(\lambda) T_k(i) \; + \; C(i) \tag{2}$$

In this fitting, a constant term $C(i)$ is still present to account for background errors, but now the constant is a function of position rather than wavelength. The spatial templates derived here, $T_k(i)$, should be similar to the initial templates $T_j(i)$, but would also identify regions where dust with a similar emission spectrum is found, but is superimposed on other emission components. The derived spatial distributions of the different characteristic spectra are shown in Figure 4.

3.3. Residuals

The total emission of each of the seven components is calculated by integrating the spectral templates, $S_j(\lambda)$ (Fig. 3), over the regions of the corresponding spatial templates, T_k (Fig. 4). Figure 5 shows the seven Cas A spectra with their actual intensities (not normalized). This comparison shows that in the ejecta, the Ar II dust component is dominant at wavelengths from 8 to 35 μm. The dust associated with the radio emission is assumed to be swept up ISM dust, and is generally $< 1/3$ of the luminosity of the ejecta dust. The sum of the all the spectra is also shown as a "fit" to the total Cas A spectrum derived without any decomposition into components. The general agreement at 10 – 35 μm indicates that there are no major missing components. At shorter and longer wavelengths, the comparison is not as good. This is primarily due to difficulties in the background subtraction when integrating over the entire area of the SNR.

Images (at selected wavelengths) of the differences between the total Cas A emission and the sum of the components are shown in Figure 6. Examination of these images and the full set of residuals at all wavelengths shows that at any chosen locations the residuals can be both positive and negative as a function of wavelength. Prior to the inclusion of the South Spot component, there was a conspicuous positive residual at nearly all wavelengths at that location. The variations of the residuals indicate that locally there are more subtle variations of the emission in the SNR than can be traced by our derived spectral templates. Such variations would be expected from small changes in the dust temperature that would be expected if the physical conditions that prevail where each type of dust is found are not strictly uniform across the SNR.

4. DUST COMPOSITIONS FOR DIFFERENT TEMPLATES

Six of the seven characteristic dust spectra show strong emission at wavelengths from 10 - 40 μm. The *Spitzer* IRS spectra across these wavelengths reveal distinctive features in each of these spectra. The features generally appear to be suggestive of silicates with peaks of varying sharpness at ~ 10 and ~ 20 μm. In order to identify the particular type of silicates and/or other grain compositions that produce each of the characteristic spectra, we assembled a set of grain emissivities from published optical constants (Table 2), and fitted each template's spectrum, $S_k(\lambda)$, as the weighted, $M_{n,i}$, sum of different grain emissivities, $\kappa_n(\lambda)$, applied to blackbody emission at different temperatures, $B(T_i)$:

$$S_k(\lambda) = \sum_n \sum_{T_i=20\mathrm{K}}^{2000\mathrm{K}} M_{n,i}\kappa_n(\lambda)B(T_i)\ . \tag{3}$$

The MPFIT code (Markwardt 2008) was used to determine coefficients $M_{n,i}$ needed to fit each of the normalized spectrum with the constraint that $M_{n,i} \geq 0$. For the purpose of fitting, the spectrum uncertainties were taken to be $\sigma_S = 0.2S$ with a floor of $\sigma_S \geq 0.01S$. In the fitting, the dust temperature is constrained to lie on a grid of values ranging logarithmically from $T = 20$ to $T = 2000$ with $\Delta \log_{10}(T) = 0.05$. Only components with intensities exceeding 10^{-4} times the peak of the fitted spectrum are kept in the final result.

For each spectrum, an initial set of fits was performed using only one dust composition, n, at a time. No single composition provided a good fit to the spectrum. The fits were repeated using all possible combinations of pairs of compositions (i.e. the left summation in Equation 3 is over $n = 0, 1$). Some combinations explored in this way result in substantial improvements in the fits. Usually the improved fits involved the pairing of a dust composition with strong spectral features with another composition that is relatively "featureless." Thus, we also performed a set fits using 3 compositions, but with the constraint that one was required to have a "featureless" emission spectrum. Since all the featureless compositions produce similar results, we chose the "ac" amorphous carbon composition for the fixed third component in these tests.

The quality of the one and two component fits as measured by χ^2 is shown in Figures 7-12. The left panel of each figure shows a matrix of the χ^2 values, with generalized axes. This is useful to get an overview of which pairs of components yield provide the best fits. The general groupings are based on chemical and/or spectral similarity. The right panel of each of the figures displays the same χ^2 values but now plotted as a function of the second composition and color coded according to the first composition. This plot is more useful for illustrating the quantitative changes in χ^2 and allows specific components to be identified. The results for single composition fits correspond to the upper envelope of the curves in these plots (or the diagonal of the matrix in the left panels). Examples of the best fitting 2- and 3-composition models, as well as contrasting models that also provide reasonably good fits, are shown in Figures 14-34. The results for the 7 different spectra are discussed below.

4.1. Ar II dust

The emission associated with Ar II exhibits the sharpest peaks at 9 and 21 μm and seems to have a weaker peak at ∼12 μm. The astronomical silicate of the typical ISM does not have silicate peaks sharp enough to produce the observed features. Magnesium silicates (particularly $Mg_{0.7}SiO_{2.7}$, characterized by MgO / $SiO_2 = 0.7$) have peaks that are in roughly the right locations, but their shapes are not a good match to the data. However, when two-composition fits are performed, the addition of a second component lacking strong spectral features (e.g. graphite, amorphous C, or Al_2O_3), can smooth soften and smooth the silicate peaks to provide a much better fit to the spectrum.

The best 2-component fit (Figure 14) employs $Mg_{0.7}SiO_{2.7}$ to fit the 9 and 21 μm silicate peaks, and graphite as the featureless component that weakens the relative strength of the peaks. The fit to these peaks is very good, although the weaker 12 μm peak is not fit at all. Despite the overall good fit, the temperature components needed for the Mg silicate are somewhat suspicious. Components at 71—63K are needed to fit the 21 μm feature, but are too cold to contribute to the 9 μm feature. Conversely a 500 K component produces the 9 μm peak while contributing little to the 21 μm peak. Small, stochastically heated grains might be expected to be heated to this range of temperatures, but it is problematic that there is no indication of grains at intermediate temperatures (70K$< T <$ 400K). This suggests that the emissivities used here are not a true physical representation of the Ar II dust. The actual dust must either have a relatively stronger 9 μm peak so that it can produce the observed spectrum from cooler dust, or it must have a somewhat lower emissivity at roughly 10-20 μm so that the presence of grains at intermediate temperatures would be required.

Figure 15 shows an alternate 2-component fit where the same Mg silicate is paired with a nonstoichiometric spinel [$Mg_xAl_yO_4$; $y = (8 - 2x)/3$]. These spinels (especially with a low Mg/Al ratio) have a spectral peak that improves the fit to the observed 12 μm feature, at the expense of poorer fits to the other silicate peaks. The maximum temperature required for the silicate grains is much lower here, but the temperature of the spinel reaches 2000K, which is the maximum value allowed. This high temperature is driven by two influences. The first is to add the 12 μm feature to the spectrum without making significant contributions at longer wavelengths. The second is to provide the (uncertain) continuum level at < 8 μm. The fits are not seriously worse if the maximum temperature is restricted to a lower value (e.g. 400K).

As suggested by the previous 2-component fits, the best 3-component fit combines the $Mg_{0.7}SiO_{2.7}$ with a featureless amorphous C (to weaken the silicate peaks) and a nonstoichiometric spinel to provide the 12 μm peak (Fig. 16). However there is still a tendency in this fit to use distinctly different temperature and/or composition components to fit each different spectral feature. The spinel material that produces the 12 μm peak is still required to be at extremely high temperatures. Alternate sources of the 12 μm feature are SiO_2 and SiC. For both of these materials, the spectral features are too sharp and slightly too blue to provide a good match when the mass absorption coefficients,$\kappa(\lambda)$ are calculated from Mie theory for spherical grains. However, calculations assuming a continuous distribution of ellipsoids (CDE) for particle shapes, result in spectral features that are broader and redder. The dust temperatures required to produce the features are also much more reasonable. Figures 17 and 18 show the fits when CDE calculations are used for a third composition of SiO_2 or α-SiC. SiO_2 provides some contribution to all three of the observed peaks. SiC only provides the 12 μm peak.

4.2. Ar III dust

The Ar III dust spectrum is very similar to that of the Ar II dust. It was derived separately to check if there might be an identifiable shift in dust temperature or composition in these closely related regions. Not surprisingly, the combinations that produced good fits to the Ar II spectrum also produce good fits to the Ar III spectrum (Figures 19–16). This increased strength of the 9 μm peak relative to the 21 μm peak would usually suggest warmer dust temperatures in association with the Ar III. However, because the dust features arise largely from separate components of the models, the temperature of the components are largely unchanged, but the relative mass in the hotter components is higher for the Ar III than for the Ar II spectrum.

For the Ar III spectrum we consistently find that the amorphous C (ac) provides a slightly better fit than the graphite that was somewhat preferred for Ar II spectrum. The Ar III spectrum is also slightly better fit when hibonite rather than the spinels is used as a third component, although if CDE calculations are applied, SiO_2 and SiC can again provide equally good fits as the third component.

4.3. Ne II dust

The dust associated with Ne II exhibits an unusually smooth spectrum. This spectrum excludes significant amounts of warm silicates, but can be fit by compositions with relatively featureless spectra, e.g. graphite, and amorphous carbon. The best fits are found by combining featureless dust with Al_2O_3. The latter component has a very broad emission peak between 10 and 20 μm that improves the fit. Figure 22 shows the fit for an amorphous carbon (be) – Al_2O_3 mixture. The fit suggests that some fraction of the Al_2O_3 component is fairly warm ($T \approx 150$ K), while the brightest carbon dust has a temperature of ~ 75 K. A significant cool (~ 40 K) dust component helps to fit the *Herschel* data at 70 – 160 μm. The model attributes this to Al_2O_3, but this identification is degenerate because neither of these compositions have any characteristic spectral features at these wavelengths. The composition of very cool components cannot be identified very conclusively, because the shape of the spectra are hardly affected by composition.

Figure 23 shows the best fit model that does not contain Al_2O_3. In this case a nonstoichiometric spinel provides a relatively small perturbation to an otherwise smooth amorphous C spectrum. Amorphous C picks up the intermediate temperature ($\sim$ 135K) components that account for the bulk of the 10 – 20 μm emission.

Figure 24 shows the best 3-component model for the Ne II dust. The addition of TiO_2 nominally improves the fit over the best 2-component model, but the changes to the spectrum are too minor to suggest that any third component is warranted.

4.4. X-Ray Fe dust

The spectrum of dust associated with the X-ray Fe emission does exhibit apparent silicate peaks at $\sim$ 10 and 20 μm. The 10 μm peak is relatively weak, suggesting a lack of hot silicate grains. As with the Ar II dust, mixing silicate and more featureless emission (e.g. amorphous C) improves the quality of the fit. The preferred silicates here tend to have higher MgO/SiO_2 ratios than those that fit the Ar II and Ar III dust. Figure 25 shows the best 2–composition fit. The temperatures for both components are warm, $T \approx 100 - 112$ K, with additional hot and cold components to account for the short and long wavelength emission. Figure 26 shows the best 2–component fit that is obtained without the use of silicate compositions. This marginal fit uses $Mg_{0.6}Fe_{0.4}O$ to adjust the shape of the model spectrum near 20 μm, but contains no replacement for a 10 μm silicate feature. The best 3–component fit (Fig. 27) merely adds PAH^+ emission to reproduce a bump at 8 μm and sharpen the spectral feature at $\sim$ 10 μm. The overall change in χ^2 is small.

4.5. South Spot dust

The South Spot spectrum looks rather different than the X-ray Fe spectrum, yet it tends to be best fit by similar dust compositions. Here the temperatures of the components that produce the $<$ 20 μm emission are higher than those for the X-ray Fe dust. Figure 28 shows the best 2–component fit which uses similar compositions as the X-ray Fe spectrum (cf. Fig. 25). Figure 29 shows a marginal fit obtained without the use of silicates, and thus without any component that provides a 10 μm feature in the spectrum. The best 3–component fit (Fig. 30) uses nonstoichiometric spinel to make minor adjustments to the shape of a good 2–component model.

4.6. Radio (ISM) dust

As for the X-ray Fe and South Spot spectra, the spectrum associated with the radio emission tends to be best fit with a mix of silicate and featureless dust. Figure 31 shows the best 2–composition fit. Figure 32 shows a marginal 2–composition fit, in which $Mg_{0.1}Fe_{0.9}S$ serves as the “featureless” component across the 10–20 μm part of the spectrum. The best 3–component fit (Fig. 33) is not significantly different from the best 2-component fit, using two featureless components instead of one. Figures 34 shows the best results when dust compositions are restricted to the astronomical silicate, graphite, PAH and PAH^+, which are commonly used to fit general interstellar material (e.g. Zubko et al. 2004). The shape of the astronomical silicate’s 10 μm emission peak is not as sharp as the observed spectrum. Cool PAH^+ emission provides sufficient adjustment to the shape of the silicate spectrum such that the model does not require and graphite or neutral PAH components.

4.7. Si II dust

The Si II dust spectrum essentially contains only the *Herschel* PACS measurements at 70, 100, and 160 μm, with only upper limits on the emission at shorter wavelengths. Because of this lack of detailed spectral information, the spectrum was only fit with single composition dust models. The Si II spectrum has a relatively sharp peak compared to a black body spectrum. The best fit is provided by $CaAl_{12}O_{19}$ which has a broad emission feature at ~ 80 μm making it an especially good fit to the data. Figures 35 and 36 show the best fit spectrum ($CaAl_{12}O_{19}$), and a fit using a more typical Mg silicate (Mg_2SiO_4). Compositions that have a steeper spectral index at long wavelengths provide better fits, but the relatively good fit for TiO_2 (3) (rutile) is an artifact of an unphysically steep extrapolation ($\lambda^{-3.5}$) implied by the measured optical constants, limited to < 35 μm. For the Si II spectrum, any models that are within a factor of 4 of the minimum χ^2 are deemed acceptable. This includes most dust compositions, and only excludes compositions that have strong features near ~ 40 μm that would have exceeded the upper limits provided by the *Spitzer* IRS data.

5. DISCUSSION

The identifications of possible dust compositions in the different environments in Cas A are summarized in Table 3. A single dust composition can never provide a good fit to the observed spectra, except for the Si II spectrum which has only upper limits at < 70 μm. In general, 2 compositions are sufficient to get acceptable fits to the spectra. The Ar II and Ar III spectra are the only ones that show significant (though small) benefit for the addition of a third composition. Among the 7 characteristic dust spectra examined, the results can be grouped into 3 different families of dust.

The first family is found in association with the Ar II and Ar III emitting ejecta, which are distributed widely across the SNR. This family consists of the "lightest" Mg silicate (i.e. lowest MgO/SiO_2 ratio) in combination with one or more other compositions that have a featureless spectrum. The $Mg_{0.7}SiO_{2.7}$ is a good fit to the 9 and 21 μm peaks in the observed spectrum, but only if a featureless dust composition is also present to reduce the apparent strength of these features. However, the Ar dust spectra also contain a weaker 12 μm feature which is not accounted for by any Mg silicate. Nonstoichiometric spinel with low Mg/Al ratios can provide a feature at approximately the correct wavelength, but only when the dust grains are extremely hot, such that longer wavelength spinel features are relatively faint. A better explanation for the 12 μm feature may be provided by SiO_2. The spectrum of SiO_2 exhibits exhibits all three peaks seen in Ar II and Ar III spectra, although they are are significantly sharper and slightly bluer than the observed ones, and even in combination with other materials the fits are not very good. However, this is when Mie theory is used to calculate the absorption cross sections assuming small spherical grains. Using a continuous distribution of ellipsoids (CDE) approximation instead, broadens and shifts the

SiO_2 features to be a better match as a third component. Jäger et al (2003) point out that the 12 μm SiO_2 feature disappears in Mg silicates when $MgO/SiO_2 > 0.5$. Therefore, it seems likely that the dust associated with the Ar emission is a Mg silicate – silica mix with $MgO/SiO_2 \lesssim 0.5$ in combination with a separate featureless dust component. SiC can also provide the 12 μm feature, but again only if CDE calculations are applied to this component. If SiC is present, this would be the only direct evidence of carbon-bearing dust. Table 4 lists the possible origins for the 12 μm feature of the Ar dust.

The strong 21 μm peak in this family has been the hallmark of Cas A IR spectra since it was first observed using KAO and ISO. On the basis of those data, the peak was suggested to arise from Mg protosilicate (Arendt et al 1999). Subsequent analysis by Douvion et al. (2001) modeled an *ISO* spectrum as $MgSiO_3$, SiO_2 and Al_2O_3 with the weak 12 μm feature largely produced by the Al_2O_3 as proposed for the feature in "Spectrum 2" of Douvion et al. (1999). Ennis et al. (2006) using *Spitzer* IRS data noted the distinction of several different dust spectra in different parts of Cas A and referred to this as the "Strong 21 μm" spectrum, and Rho et al. (2008; calling it "21 μm peak dust") modeled it as Mg protosilicate and $MgSiO_3$ with secondary components of SiO_2, FeO, FeS, Si, Al_2O_3 or FeO, SiO_2, FeO, FeS, Si, Fe.

The second dust family is associated with the Ne II emission, which is especially prominent in two opposing "Ne crescents" (Ennis et al. 2006; Smith et al. 2009) in the N and S parts of the SNR. These morphological features are evident in the distribution of the Ne II dust shown in Figure 4. This dust has a very smooth spectrum that does not suggest any silicate material. The best fits to the spectrum are found with Al_2O_3 in combination with other featureless dust. Featureless dust alone can provide moderately good fits, but a broad asymmetric feature in the 10 – 20 μm portion of the Al_2O_3 absorption cross section seems to match the observed spectrum especially well. Alternately, nonstoichiometric spinel can provide the needed emission at 10 – 20 μm, although the spinel emissivity has more detailed substructure that is not evident in the observed spectrum.

This second family corresponds to the "weak 21 μm" components noted by Ennis et al. (2006) and Rho et al. (2008) which they also associate with relatively strong Ne emission. However, the fact that they see even a weak 21 μm peak in their spectrum suggests that it is a mixture of what we identify as very distinct Ar and Ne dust families. As in our fitting, Rho et al. (2008) fit this spectrum with hot and cool featureless dust (C glass) and with an intermediate temperature Al_2O_3 components. They included other components to add the weak 21 μm peak that appears in their spectrum. Douvion et al. (1999) had also noted an anti-correlation between the 9 μm silicate emission and Ne II and Ne III emission.

The third dust family is associated with the X-ray Fe emission and the South Spot. This family also seems to match the dust associated with the radio emission, which is largely dust that has been swept up from the interstellar or circumstellar medium by the forward shock. The primary component in this family is one of the "heavier" Mg silicates (i.e. with high MgO/SiO_2 ratios) or MgFe silicate: Mg_2SiO_4, $Mg_{2.4}SiO_{4.4}$, $MgFeSiO_4$. Other Mg silicates with $MgO/SiO_2 \geq 1$ can provide acceptable fits, but the silicates with lower ratios that were needed for the Ar dust are not suitable here because of the changing placement and shape of the 9 and 21 μm features.

This dust family is matched by the "Broad" component identified by Ennis et al. (2006) and the "Featureless" component modeled by Rho et al. (2008). In both cases this component is *not* associated with Ar or Ne emission lines, just as we also find. Rho et al. (2008) modeled this component as $MgSiO_3$, FeS, and Si combined with Al_2O_3, Mg_2SiO_4 and/or Fe. Using 5-17 μm ISO data, Dovioun et al. (1999) extracted a spectrum ("Spectrum 3") from a region that should match our Radio spectrum. Despite the limited wavelength coverage, they also found that the spectrum could be fit with Draine & Lee astronomical silicate (but without graphite) at $T \sim 105$ K, as we confirm in Fig. 34.

The Si II dust has no significant emission across the 5-40 μm wavelength range of the IRS. The three *Herschel* PACS measurements at 70, 100, and 160 are insufficient to constrain the composition of the associated dust. The Si II dust may belong to one of the above families, or it may be an entirely different composition.

The modeled dust temperatures and compositions allow the determination of the dust mass in each of the components. Generally the dust mass is dominated by a warm component (60 - 130K) that also produces the bulk of the luminosity. However the X-ray Fe spectrum is an exception, because the *Herschel* PACS data at 70-160 μm are elevated relative to the shorter wavelength emission, which requires an additional cold component that likely dominates the mass. The composition is uncertain because emissivities are smooth and the spectral resolution is poor at the long wavelengths. This is uncertainty is worse for the Si II dust which is only detected at ≥ 70 μm. Its temperature is relatively well constrained, but its composition, and therefore its mass, is not. If the dust is composed of Mg silicates, then the total mass is $\lesssim 0.1$ $M_\odot$, but this value can be either lower or much higher if other compositions are appropriate. The derived dust masses averaged over all models that fit within a factor of 2 of the minimum χ^2 and are dominated by Mg silicates (or Al_2O_3 for the Ne II spectrum) are listed in Table 3. Figures 37–43 plot the total dust mass for *all* 2–component models as a function of χ^2 with color coding to indicate compositions and temperatures. The "good" models are within a factor of 2 of the minimum χ^2 (to the left of the dashed line). The figures show that although there are correlations between composition and temperatures, the derived mass is more strongly dependent on the composition than the temperature.

6. SUMMARY

We have decomposed the IR spectrum from Cas A into contribution from distinct regions of the remnant, comprising: the shocked CS/IS medium into which the remnant is expanding, the hot X-ray emitting gas and fine-structure IR line emitting regions that encountered the reverse shock, and unshocked regions of the ejecta. We then calculated the mass and composition of the dust associated with each region of the ejecta. The methodology and results of our paper can be briefly summarized as follows:

- We first identified a set of spatial templates representing the IR emitting regions of Cas A. These were defined by the fine structure IR lines from Ar II, Ar III, Ne II, and Si II, by the X-ray (Fe line), and by the radio synchrotron emission. The spatial templates used for the decomposition are shown in Figure 1.

- We then identified spatially distinct zones, shown in Figure 2, in which a given template emission was dominant. We then extracted the dust spectra from these zones using the procedure described in Section 3. The resulting IR spectra were assumed to represent the different spatial templates, and are presented in Figure 3. Figure 4 shows the spatial distribution of the dust associated with each of the spectral templates.

- We compiled an extensive list of dust compositions with known optical properties to calculate their contribution to the IR emission from each spatial templates. The dust species fall into 8 broad categories: silicates, protosilicates, silica, silicon carbide, carbon and metallic iron dust, aluminum oxides, oxides, and sulfides. The 59 dust compositions used in the analysis are listed in Table 2

- For each region we fitted the spectrum with all possible combinations of 2 distinct dust species, equaling a total of 59×58/2 combinations. Figures 7–13 depicts the 59×59 matrices of the χ^2 values from all the possible combinations. Figures 14–36 show how the addition of additional dust species affect the value of χ^2 for various fits to the template spectra.

- The primary dust component could be readily identified in regions that had strong IR dust features. The Ar II and Ar III ones exhibited strong IR features at 9 and 21 μm. Magnesium silicates, characterized by a MgO/SiO$_2$ stochiometric ratio of 0.7 (i.e. $Mg_{0.7}SiO_{2.7}$) provided the best fit to the spectra of these regions. The Ne II region was best fit with Al_2O_3 dust, and the X-ray Fe region, which exhibit peaks at $\sim$ 10 and 20 μm was best fit with silicates having a higher MgO/SiO$_2$ ratio of 2.4 (i.e. $Mg_{2.4}SiO_{4.4}$). A region called the South Spot had similar composition. The dust composition from the radio synchrotron emitting region was consistent with that expected from interstellar dust. The IR spectrum from the Si II emitting region arises from a cold dust component that is only seen at long wavelengths. Since very few dust compositions have distinguishing features at these wavelengths, the composition of this cold dust could not be determined.

- The secondary dust component needed to improve the fit for most regions is not uniquely identified. Table 3 lists the primary dust composition in each region in bold, and all possible secondary dust species that they need to be paired with. The secondary dust species generally have a featureless dust spectrum.

- Altogether, the IR spectrum of each of the seven regions in Cas A can be fit with two dust species. Some species are common to more than one region, so a minimal number of only

4 dust species: $Mg_{0.7}SiO_{2.7}$, $Mg_{2.4}SiO_{4.4}$, Al_2O_3, and amorphous carbon, are required to fit the entire spectrum of Cas A. These compositions suggest that the seed dust particles that formed the more complex species are MgO, SiO_2, Al_2O_3, and carbon.

- The mass of dust in the different zones is presented in Figures 37–43. The mass of dust is about 0.04 $M_\odot$ in the shocked CSM/ISM and ejecta regions, and $\lesssim 0.1$ $M_\odot$ in the unshocked ejecta characterized by the Si II emission. This dust mass is similar to that derived by Rho et al. (2008) from the *Spitzer* data, and the ~ 0.08 $M_\odot$ derived for the cold unshocked ejecta derived from the *Herschel* and *Akari* data (Barlow et al. 2010, Sibthorpe et al. 2010).
- The total mass of newly-synthesized dust ($\sim 0.1 - 0.14$ $M_\odot$) is not sufficient to account for the large amount of dust detected in high-redshift galaxies, unless the dust is not destroyed by the expanding SN blast wave in the ISM (Dwek, Galliano, & Jones 2007).

This work is based on observations made with the *Spitzer Space Telescope*, which is operated by the Jet Propulsion Laboratory, California Institute of Technology under a contract with NASA. Support for this work was provided by NASA Program NNH09ZDA001N-ADP-0032. This research made use of Tiny Tim/Spitzer, developed by John Krist for the Spitzer Science Center. The Center is managed by the California Institute of Technology under a contract with NASA This research has made use of NASA's Astrophysics Data System Bibliographic Services.

REFERENCES

Arendt, R. G., Dwek, E., & Moseley, S. H. 1999, ApJ, 521, 234

Barlow, M. J., Krause, O., Swinyard, B. M., et al. 2010, A&A, 518, L138

Begemann, B., Dorschner, J., Henning, T., et al. 1997, ApJ, 476, 199

Begemann, B., Dorschner, J., Henning, T., & Mutschke, H. 1996, ApJ, 464, L195

Begemann, B., Dorschner, J., Henning, T., Mutschke, H., & Thamm, E. 1994, ApJ, 423, L71

Braatz, A., Ott, U., Henning, T., Jäger, C., & Jeschke, G. 2000, Meteoritics and Planetary Science, 35, 75

Brandt, T. D., & Draine, B. T. 2012, ApJ, 744, 129

Chan, K.-W., Moseley, S. H., Casey, S., et al. 1997, ApJ, 483, 798

Delaney, T. A. 2004, Ph.D. Thesis, University of Minnesota

Dorschner, J., Begemann, B., Henning, T., Jaeger, C., & Mutschke, H. 1995, A&A, 300, 503

Dorschner, J., Friedemann, C., Guertler, J., & Duley, W. W. 1980, Ap&SS, 68, 159

Douvion, T., Lagage, P. O., & Cesarsky, C. J. 1999, A&A, 352, L111

Douvion, T., Lagage, P. O., & Pantin, E. 2001, A&A, 369, 589

Draine, B. T., & Lee, H. M. 1984, ApJ, 285, 89

Dwek, E., Galliano, F., & Jones, A. P. 2007, ApJ, 662, 927

Ennis, J. A., Rudnick, L., Reach, W. T., et al. 2006, ApJ, 652, 376

Fabian, D., Henning, T., Jäger, C., et al. 2001, A&A, 378, 228

Fesen, R. A., Hammell, M. C., Morse, J., et al. 2006, ApJ, 645, 283

Gordon, K. D., Engelbracht, C. W., Rieke, G. H., et al. 2008, ApJ, 682, 336

Henning, T., Begemann, B., Mutschke, H., & Dorschner, J. 1995, A&AS, 112, 143

Jäger, C., Dorschner, J., Mutschke, H., Posch, T., & Henning, T. 2003, A&A, 408, 193

Jaeger, C., Mutschke, H., Begemann, B., Dorschner, J., & Henning, T. 1994, A&A, 292, 641

Jiang, B. W., Zhang, K., & Li, A. 2005, ApJ, 630, L77

Krause, O., Birkmann, S. M., Usuda, T., et al. 2008, Science, 320, 1195

Li, A., & Draine, B. T. 2001, ApJ, 554, 778

Markwardt, C. B. 2009, Astronomical Data Analysis Software and Systems XVIII, 411, 251

Mutschke, H., Andersen, A. C., Jäger, C., Henning, T., & Braatz, A. 2004, A&A, 423, 983

Mutschke, H., Posch, T., Fabian, D., & Dorschner, J. 2002, A&A, 392, 1047

Philipp, H. R. 1985, in Handbook of Optical Constants of Solids, ed. E. D. Palik, (San Diego, CA: Acedemic Press), 749

Posch, T., Kerschbaum, F., Fabian, D., et al. 2003, ApJS, 149, 437

Reed, J. E., Hester, J. J., Fabian, A. C., & Winkler, P. F. 1995, ApJ, 440, 706

Rest, A., Foley, R. J., Sinnott, B., et al. 2011, ApJ, 732, 3

Rinehart, S. A., Benford, D. J., Cataldo, G., et al. 2011, Appl. Opt., 50, 4115

Rho, J., Kozasa, T., Reach, W. T., et al. 2008, ApJ, 673, 271

Sibthorpe, B., Ade, P. A. R., Bock, J. J., et al. 2010, ApJ, 719, 1553

Smith, J. D. T., Rudnick, L., Delaney, T., et al. 2009, ApJ, 693, 713

Zeidler, S., Posch, T., Mutschke, H., Richter, H., & Wehrhan, O. 2011, A&A, 526, A68

Zinner, E. 2008, PASA, 25, 7

Zubko, V., Dwek, E., & Arendt, R. G. 2004, ApJS, 152, 211 (ZDA)

This preprint was prepared with the AAS LaTeX macros v5.2.

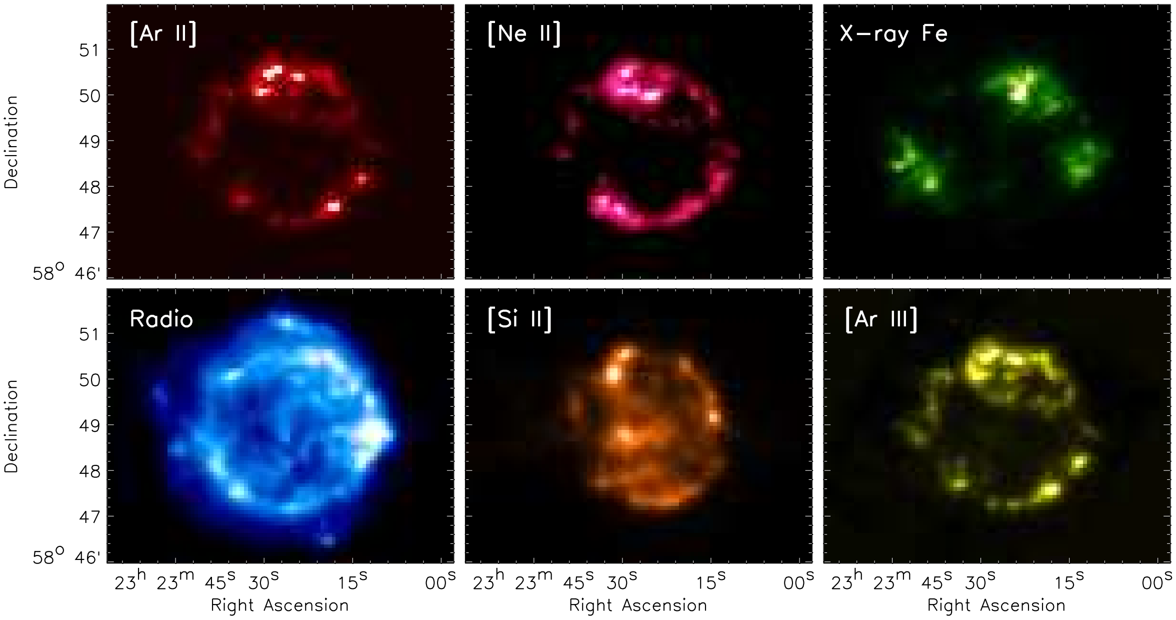

Fig. 1.— Spatial templates used for the spectral decomposition. The [Ar II] 6.99 μm, [Ne II] 12.81 μm, [Si II] 34.8 μm, [Ar III] 8.99 μm lines are derived from the IRS data cube. The X-ray Fe emission is from Hwang et al. (????) and the VLA 6 cm radio map is from DeLaney (2004).

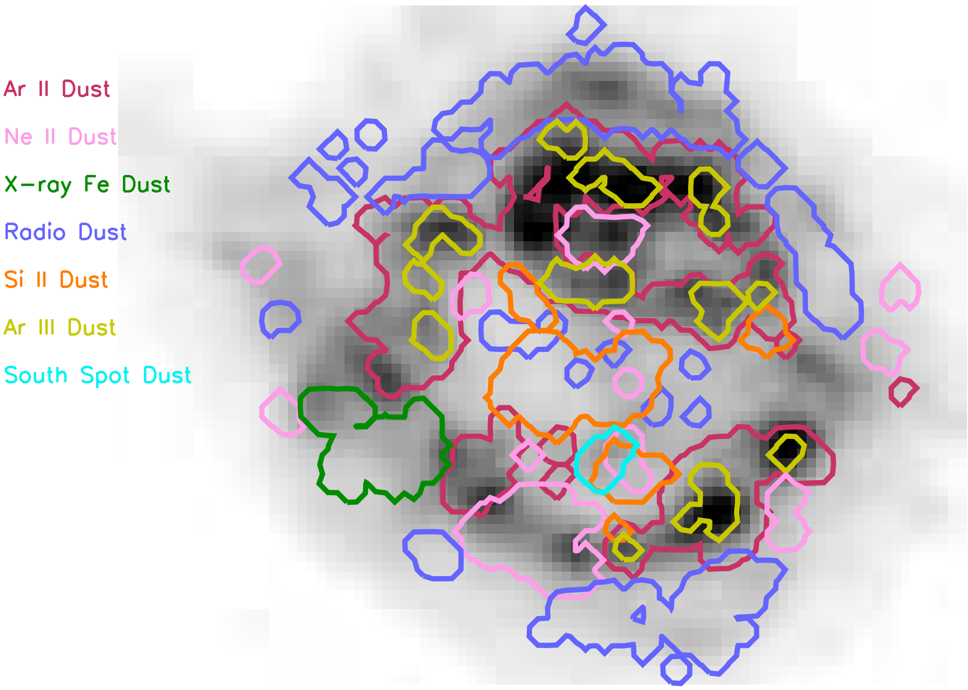

Fig. 2.— Depiction of the zones for which the different spectra were extracted. These zones correspond to the regions where the templates shown in Figure 1 are dominant (apart from the nearly ubiquitous Ar II). The additional "South Spot" zone was identified as the primary region where there is relatively strong continuum emission that is not traced by any of the spatial templates.

Fig. 3.— The continuum spectra extracted for each of the spectral zones defined in Figure 2. The solid line is the IRS data. The three points at 70, 100, and 160 μm are broadband *Herschel* PACS data.

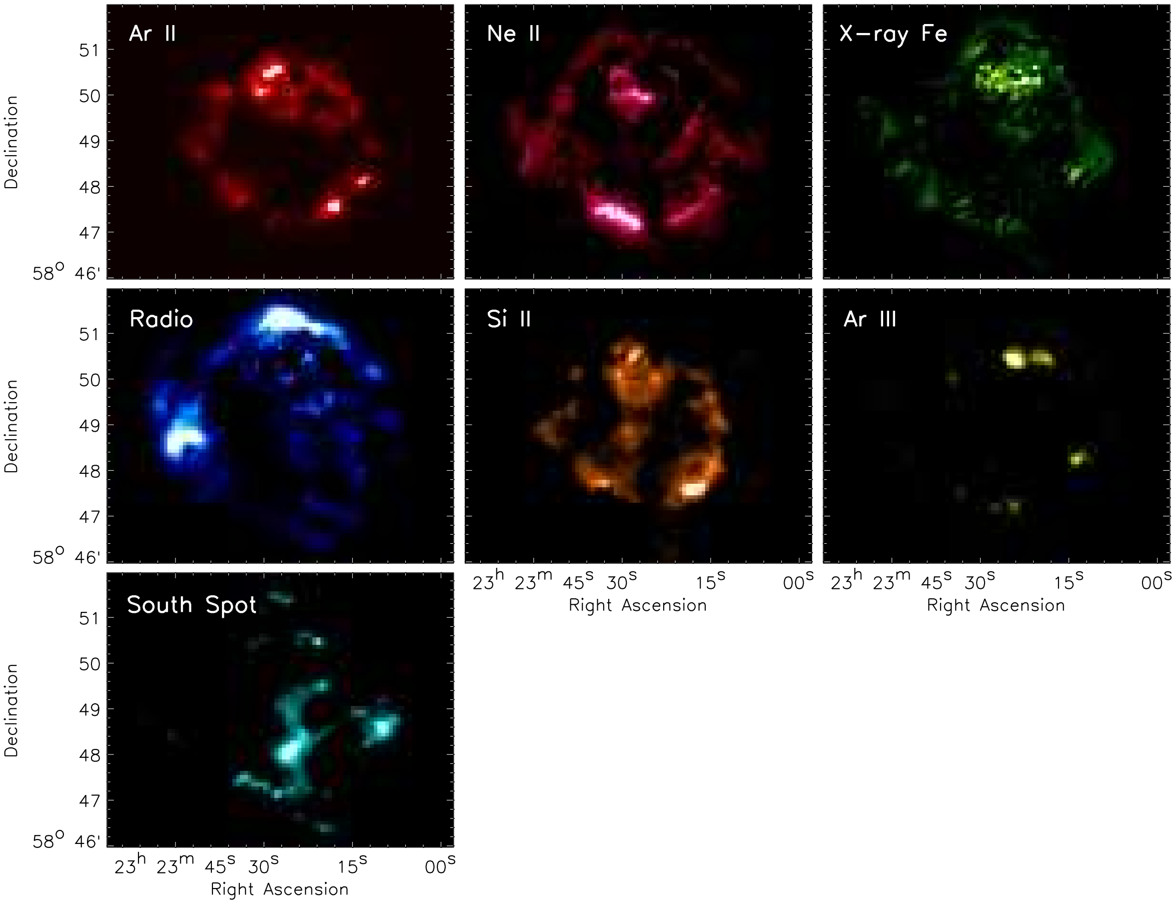

Fig. 4.— Distribution of the dust associated with each of the extracted spectral types shown in Figure 3.

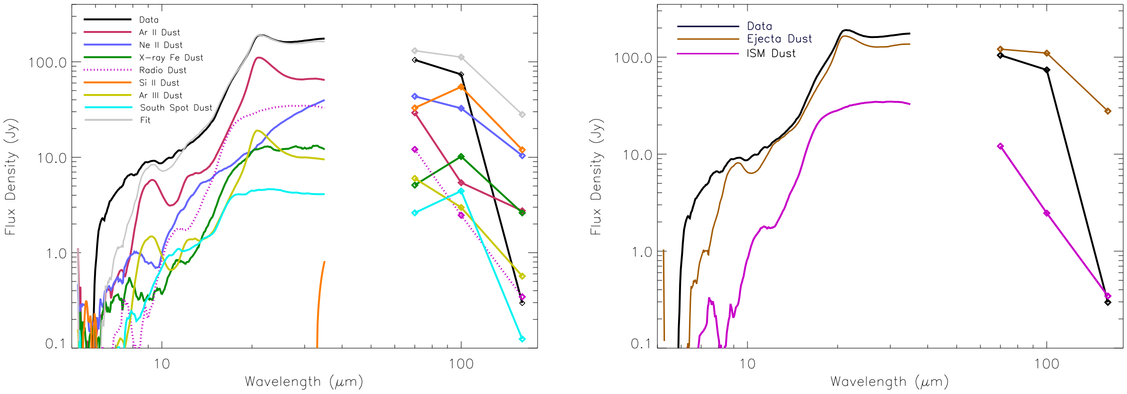

Fig. 5.— (left) Comparison of the relative intensities of each of the spectral types with the total emission of Cas A. The gray line labeled “Fit” is the sum of all the component types. (right) Comparison of the total Cas A emission with the sum of all the ejecta dust components and the ISM dust component. The ISM dust component is that associated with the radio emission of the forward shock.

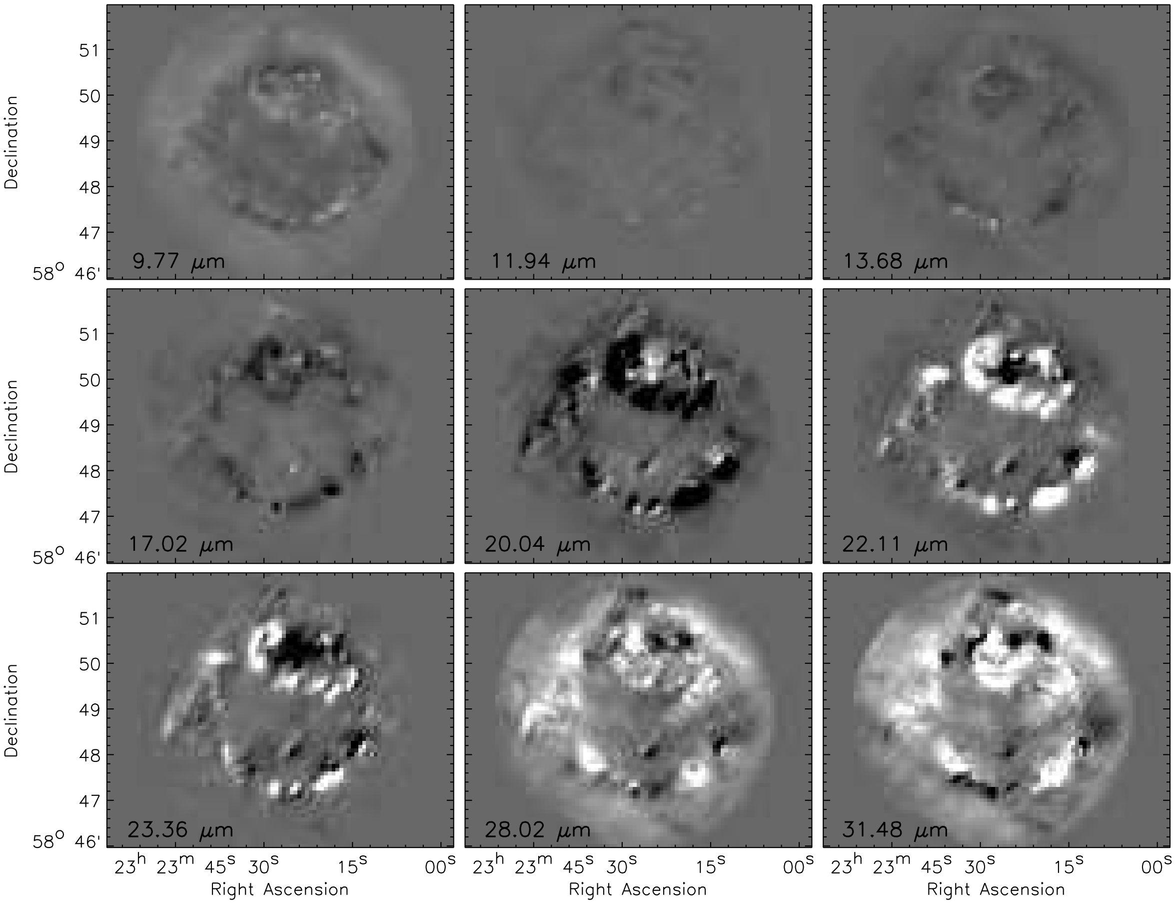

Fig. 6.— Images of the residual emission at select wavelengths in the IRS spectral cube after subtraction of the sum of the dust components shown in Figures 3 and 4.

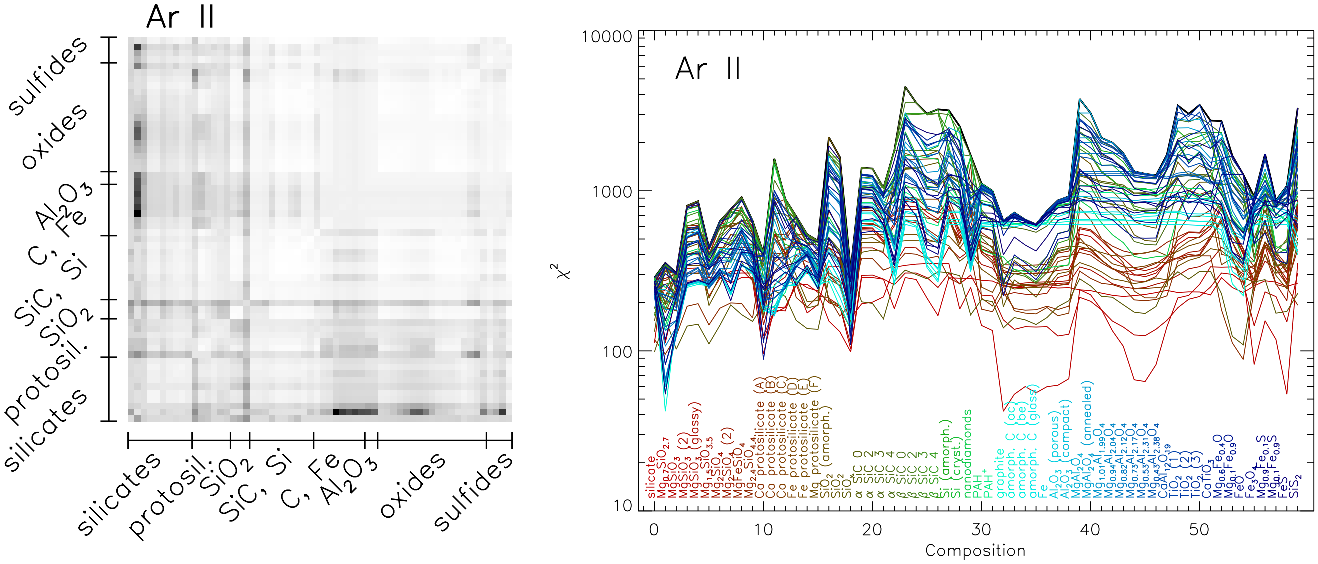

Fig. 7.— (left) A map of χ^2 for 2-composition models of the Ar II dust spectrum. Darker shading indicates lower values. The map shows that the lowest values of χ^2 are achieved when one of the silicates (second row from bottom) is paired with the relatively featureless dust such as C, Fe, Al_2O_3. Good fits are also obtained by pairing this silicate with nonstoichiometric spinels ($MgAl_2O_4$, i.e. oxides) with low Mg/Al ratios. (right) In this alternate depiction of χ^2 for 2-composition models, each line plotted shows χ^2 for a given "primary" dust component (as coded by line/label colors) when paired with each possible "secondary" component (as listed in order along the abscissa). Thus each plotted line corresponds to a row in the matrix shown to the left. Here one can see more specifically that $40 < \chi^2 < 80$ for $Mg_{0.7}SiO_{2.7}$ when paired with the relatively featureless graphite, amorphous C, Fe, Al_2O_3, Fe_3O_4, and FeS, or with the nonstoichiometric spinels with low Mg/Al ratios.

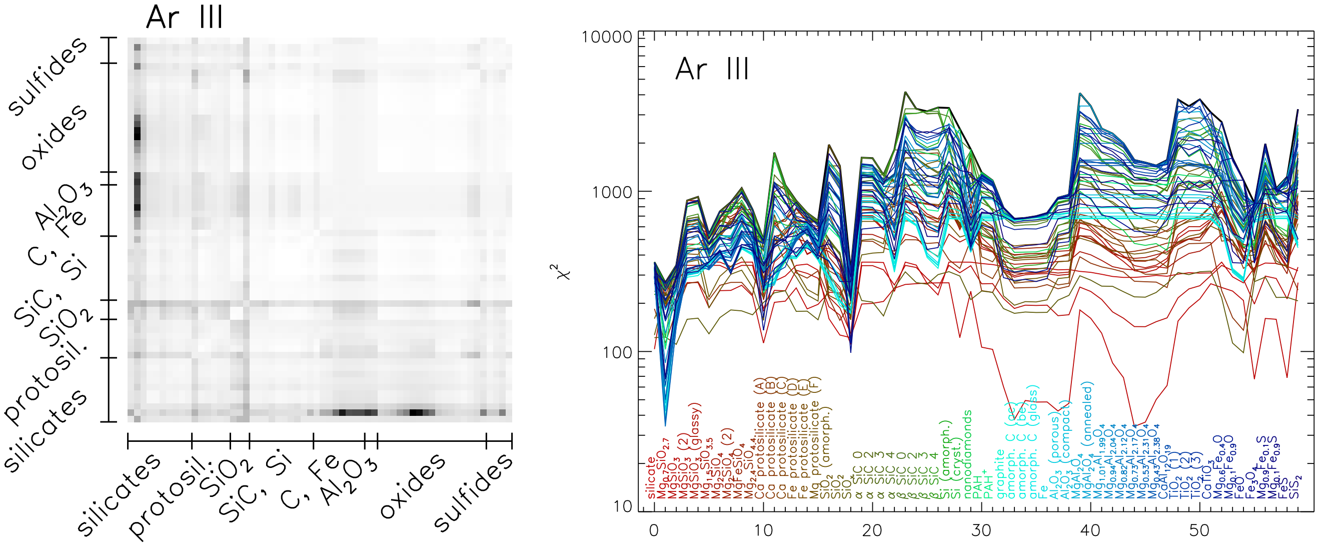

Fig. 8.— χ^2 as in Fig. 7, but for the Ar III dust spectrum. Because the Ar III dust spectrum is very similar to the Ar II dust spectrum, χ^2 for each pair of compositions is very similar in both cases.

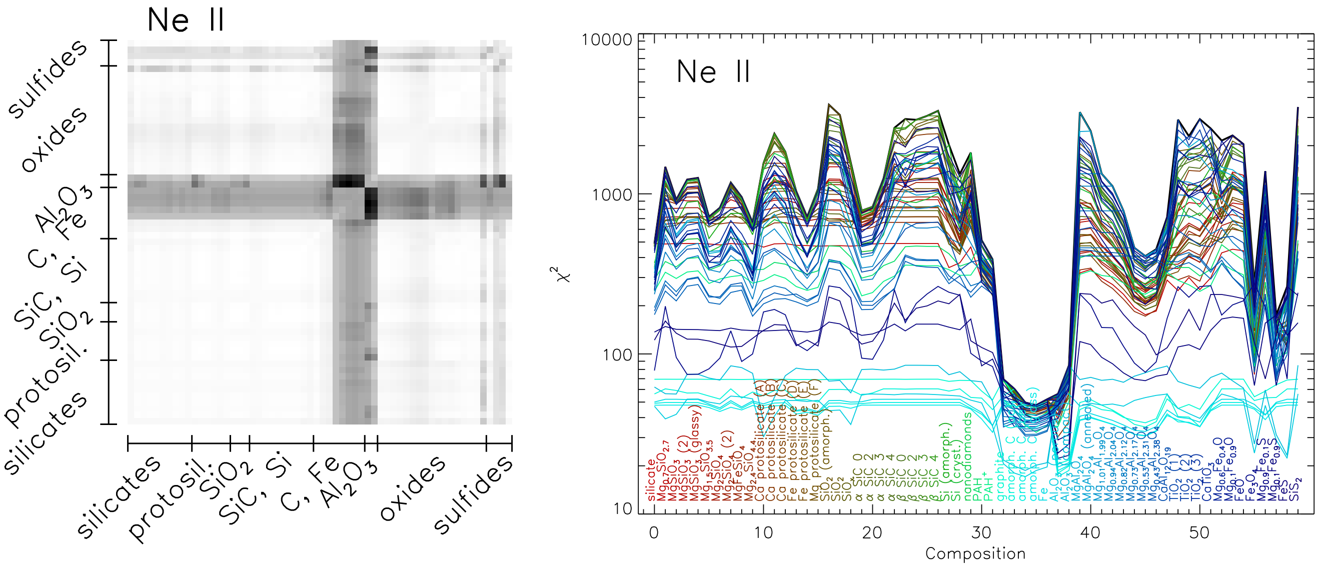

Fig. 9.— χ^2 as in Fig. 7, but for the Ne II dust spectrum. The best models contain either porous or compact Al_2O_3 paired with any of the more featureless dust components.

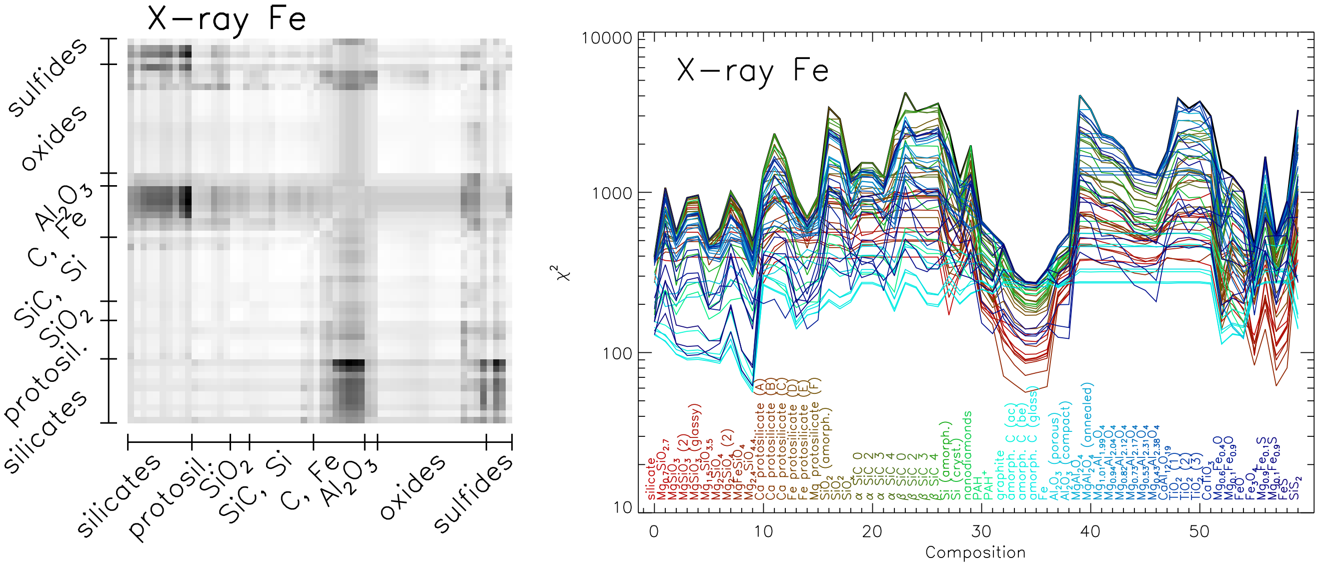

Fig. 10.— χ^2 as in Fig. 7, but for the X-ray Fe dust spectrum. This spectrum is best fit by silicates with high MgO/SiO$_2$ ratios and paired with the relatively featureless compositions.

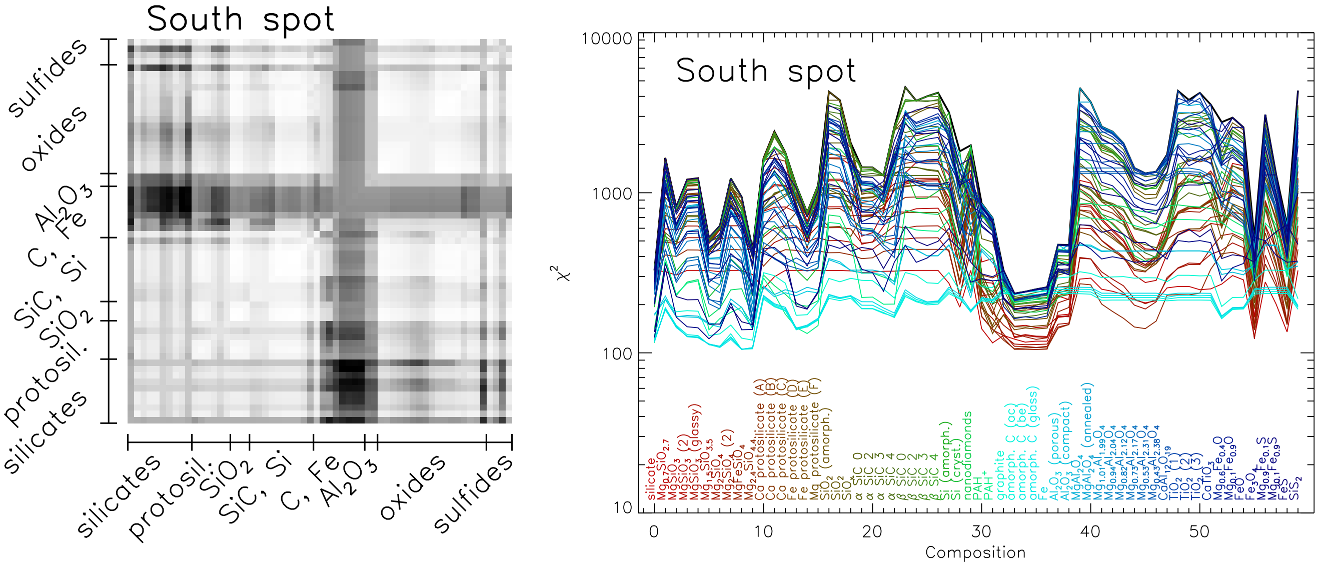

Fig. 11.— χ^2 as in Fig. 7, but for the South Spot dust spectrum. The results here are very similar to those for the X-ray Fe spectrum, but with somewhat less contrasts between the best fits and the more marginal ones.

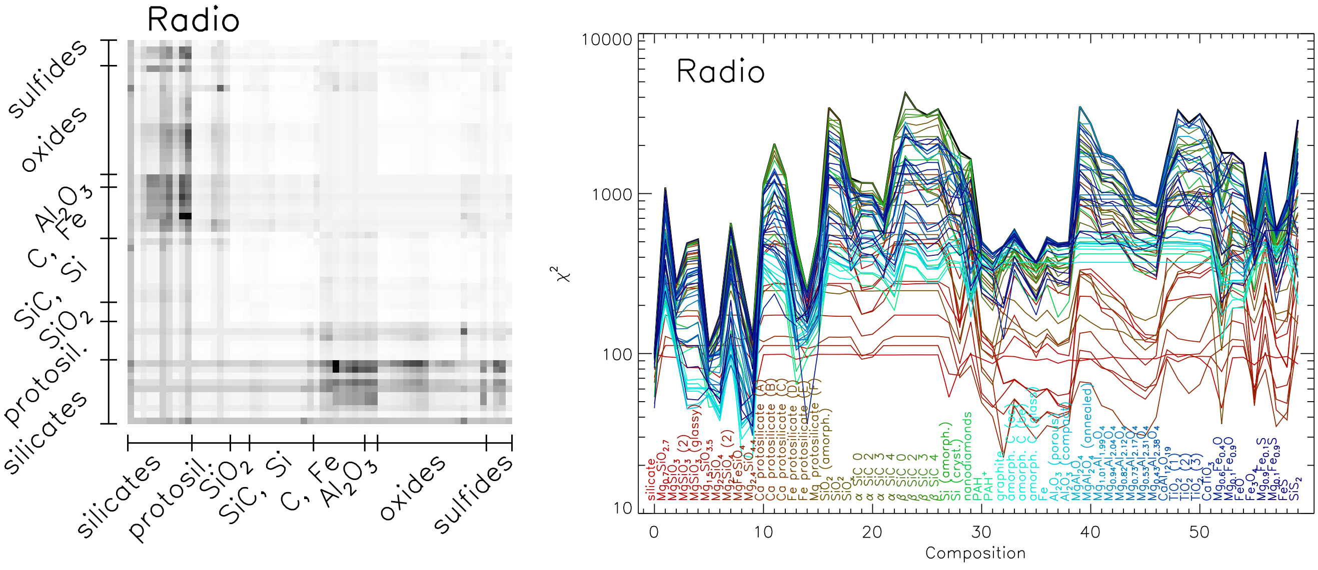

Fig. 12.— χ^2 as in Fig. 7, but for the Radio dust spectrum. The best fits here are for silicates with high MgO/SiO$_2$ ratios paired with the more featureless compositions.

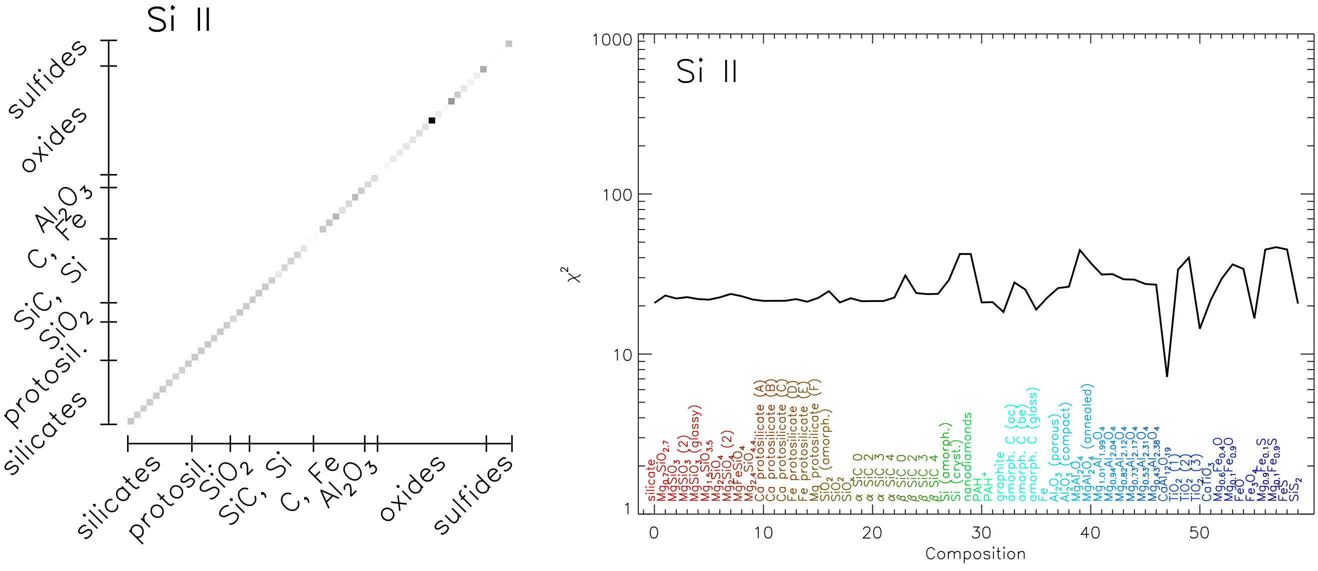

Fig. 13.— χ^2 as in Fig. 7, but for the Si II dust spectrum. Only single composition fits were performed because of the lack of detailed spectral constraints. The best fits are for compositions that have steeper long wavelength emissivities, and for hibonite ($CaAl_{12}O_{19}$) which has a broad feature at $\sim 80\ \mu$m.

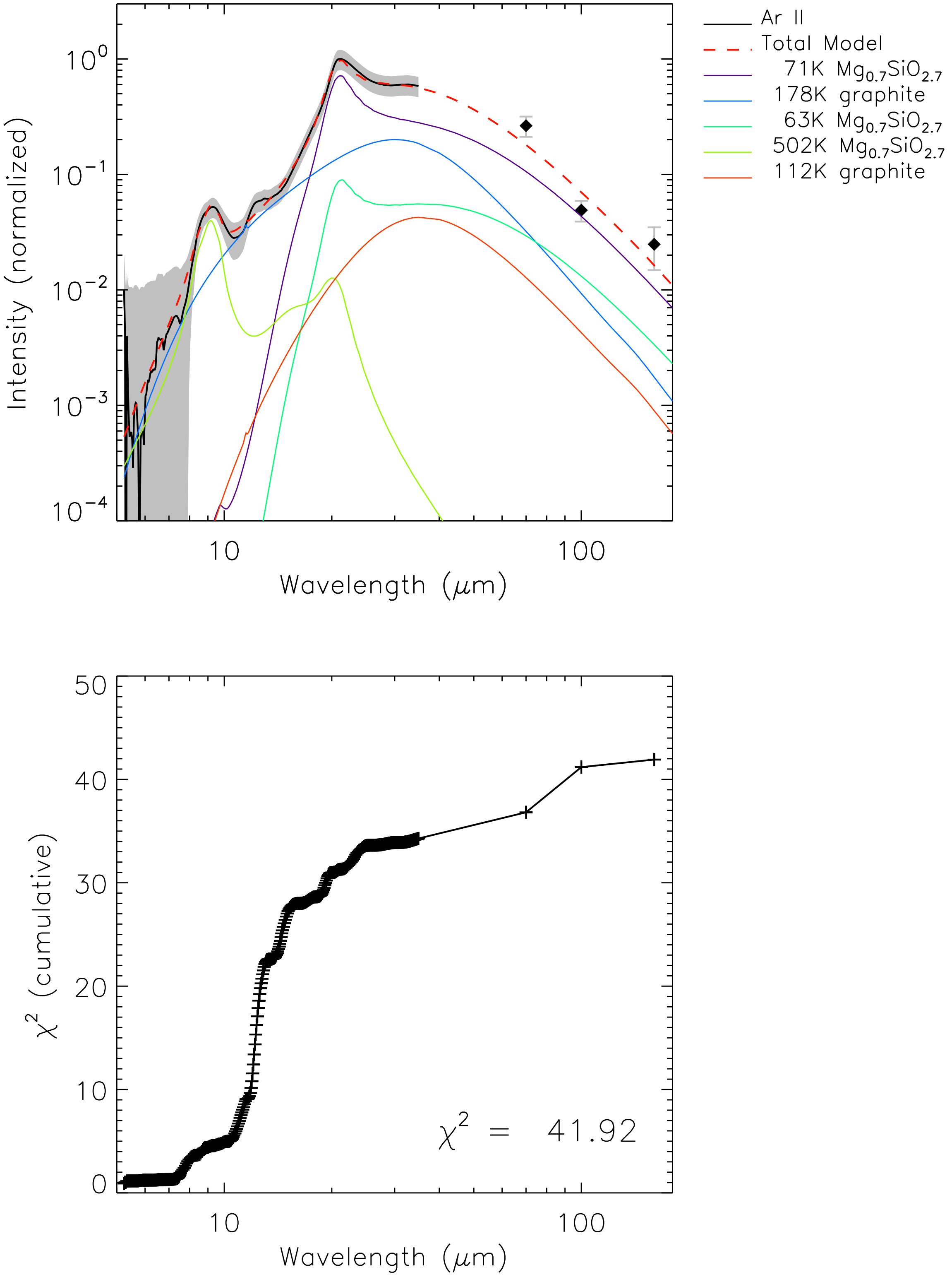

Fig. 14.— The best 2-composition fit to the Ar II spectrum includes $Mg_{0.7}SiO_{2.7}$ and a featureless dust composition.

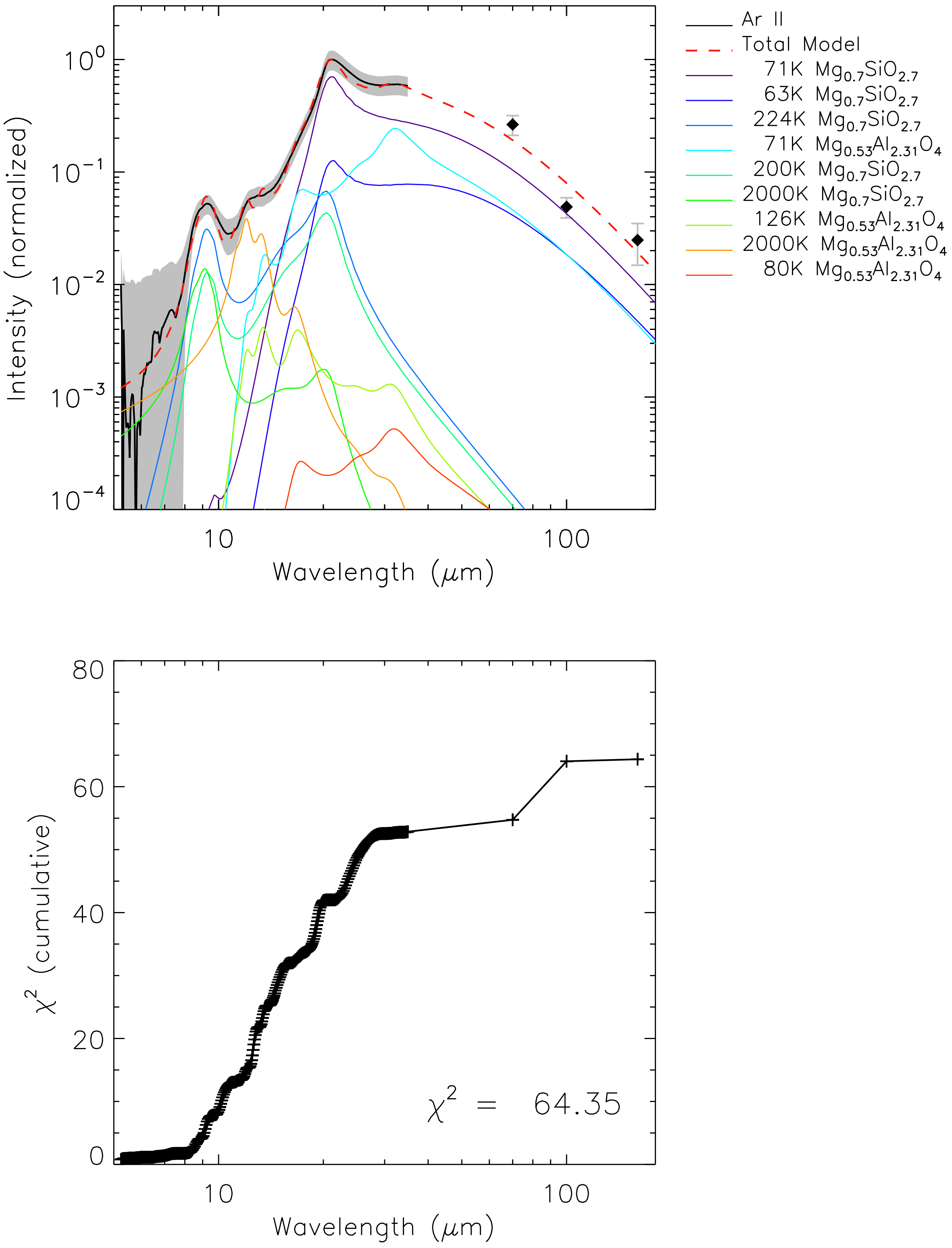

Fig. 15.— An alternate 2-composition fit to the Ar II spectrum. Here the nonstoichiometric spinel provides the unusual bump at 12 μm.

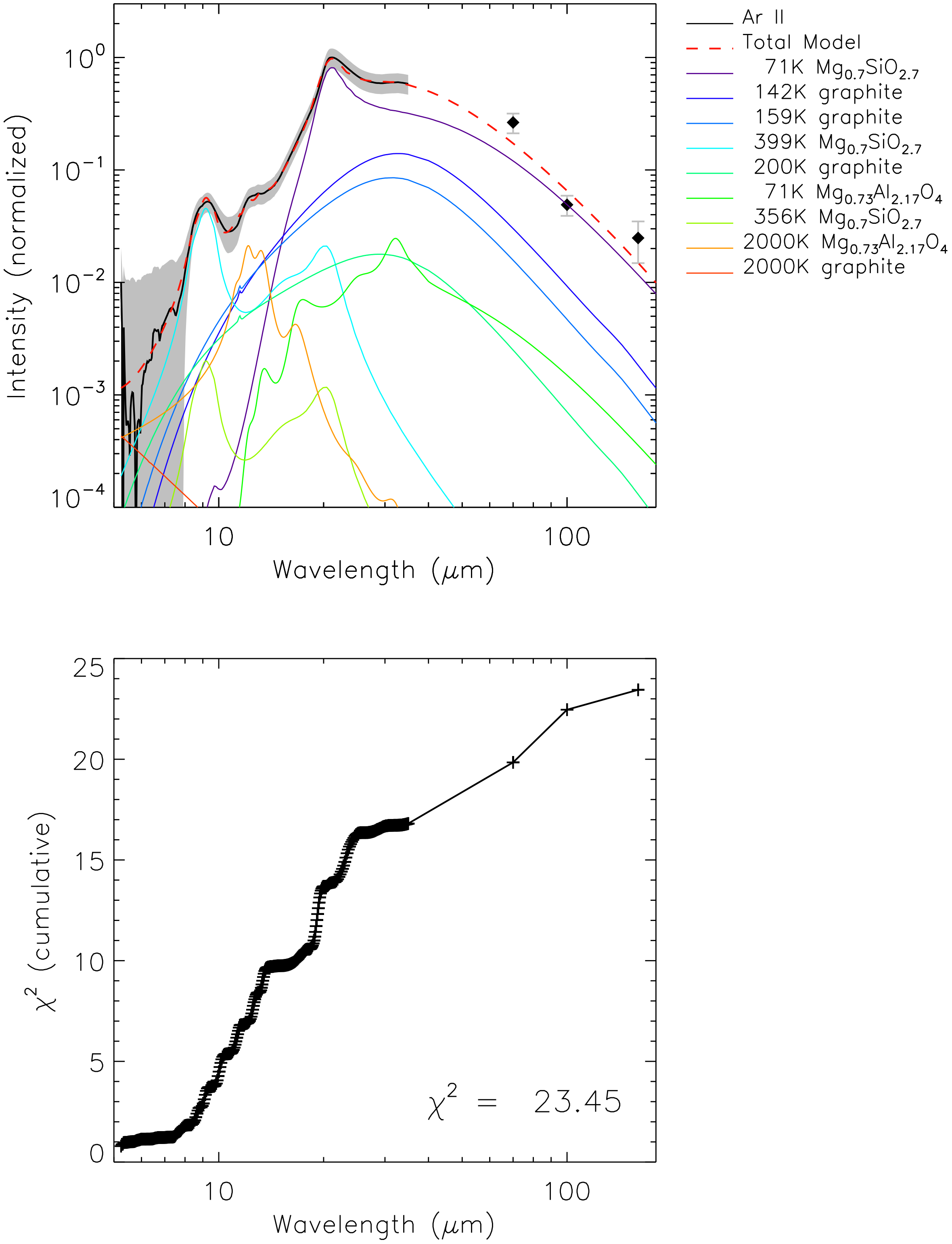

Fig. 16.— The best 3-component fit to the Ar II spectrum is a good match to all of the features at 9, 12 and 21 μm. However, the 12 μm feature is provided by implausibly hot nonstoichiometric spinel.

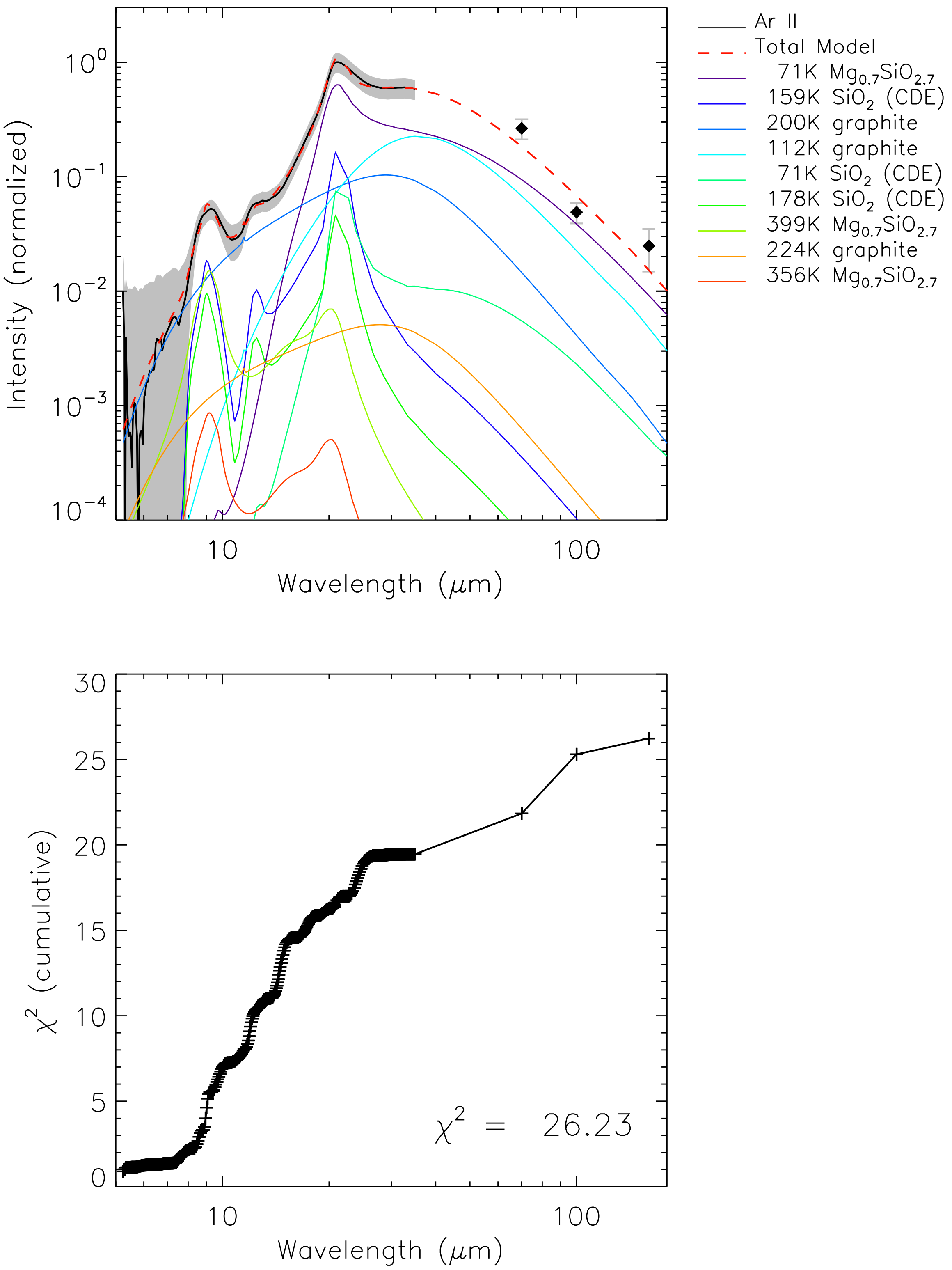

Fig. 17.— A very good 3-component fit to the Ar II spectrum can also be obtained with SiO_2 as the third component if its mass absorption coefficient is calculated via CDE rather than Mie theory. SiO_2 has features at each of the observed peaks.

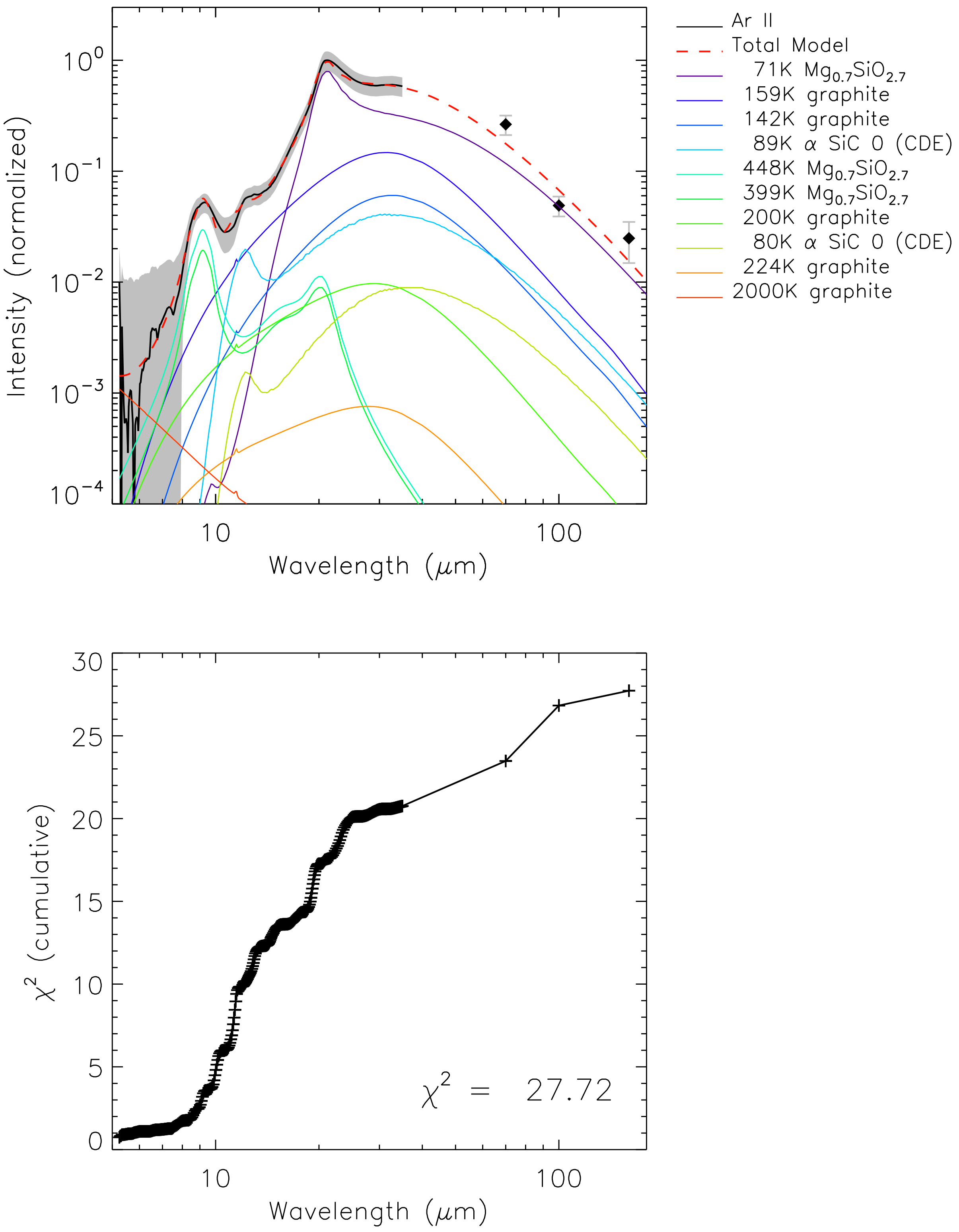

Fig. 18.— A very good 3-component fit to the Ar II spectrum can also be obtained with SiC as the third component if its mass absorption coefficient is calculated via CDE rather than Mie theory. SiC contributes only at 12 μm, but may also provide a partial match of the 21 μm feature (Jiang et al. 2005).

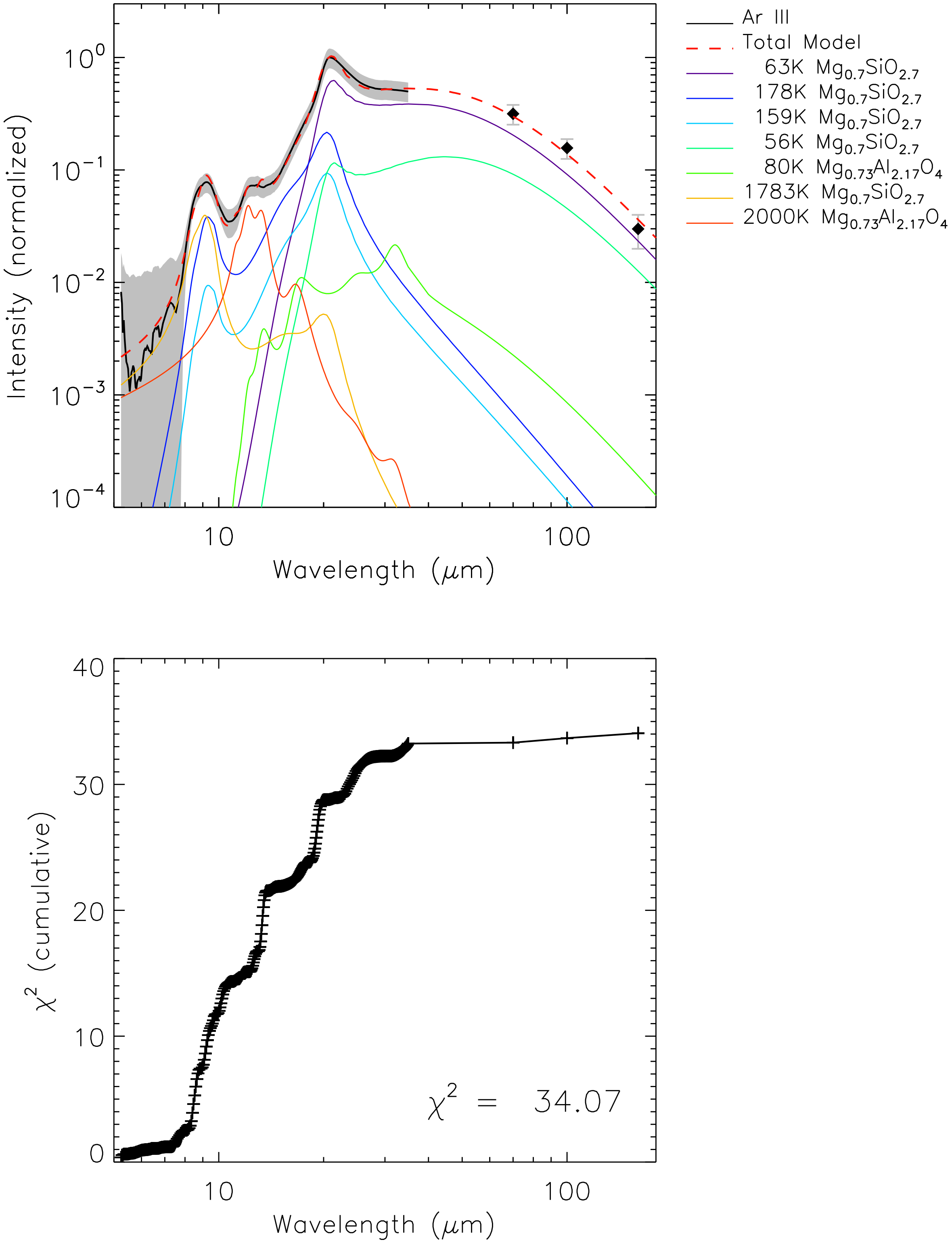

Fig. 19.— The best 2-composition fit to the Ar III spectrum makes use of the 12 μm feature of nonstoichiometric spinel.

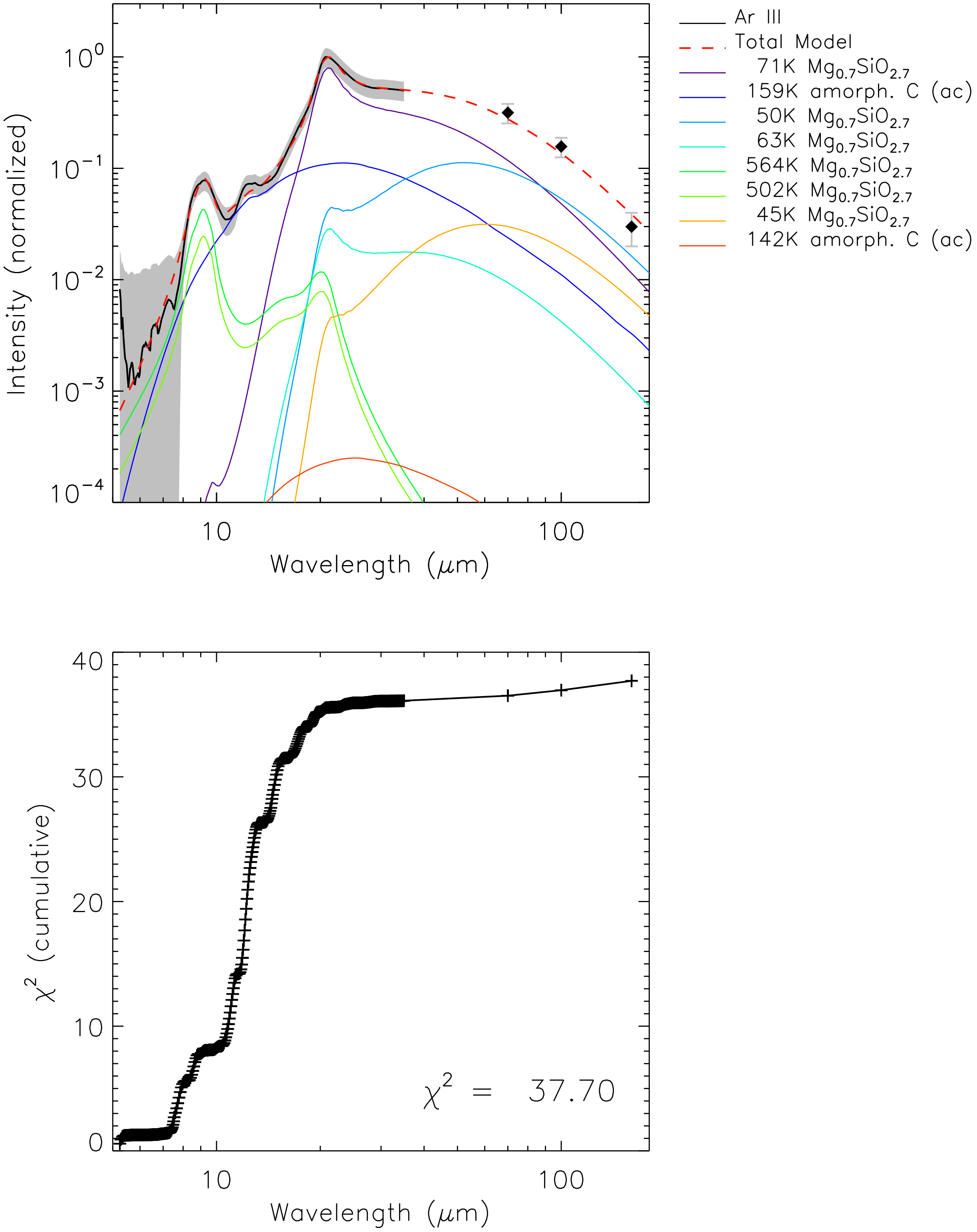

Fig. 20.— Alternate 2-component fits to the Ar III spectrum using featureless compositions fit nearly as well, but do not match the 12 μm peak.

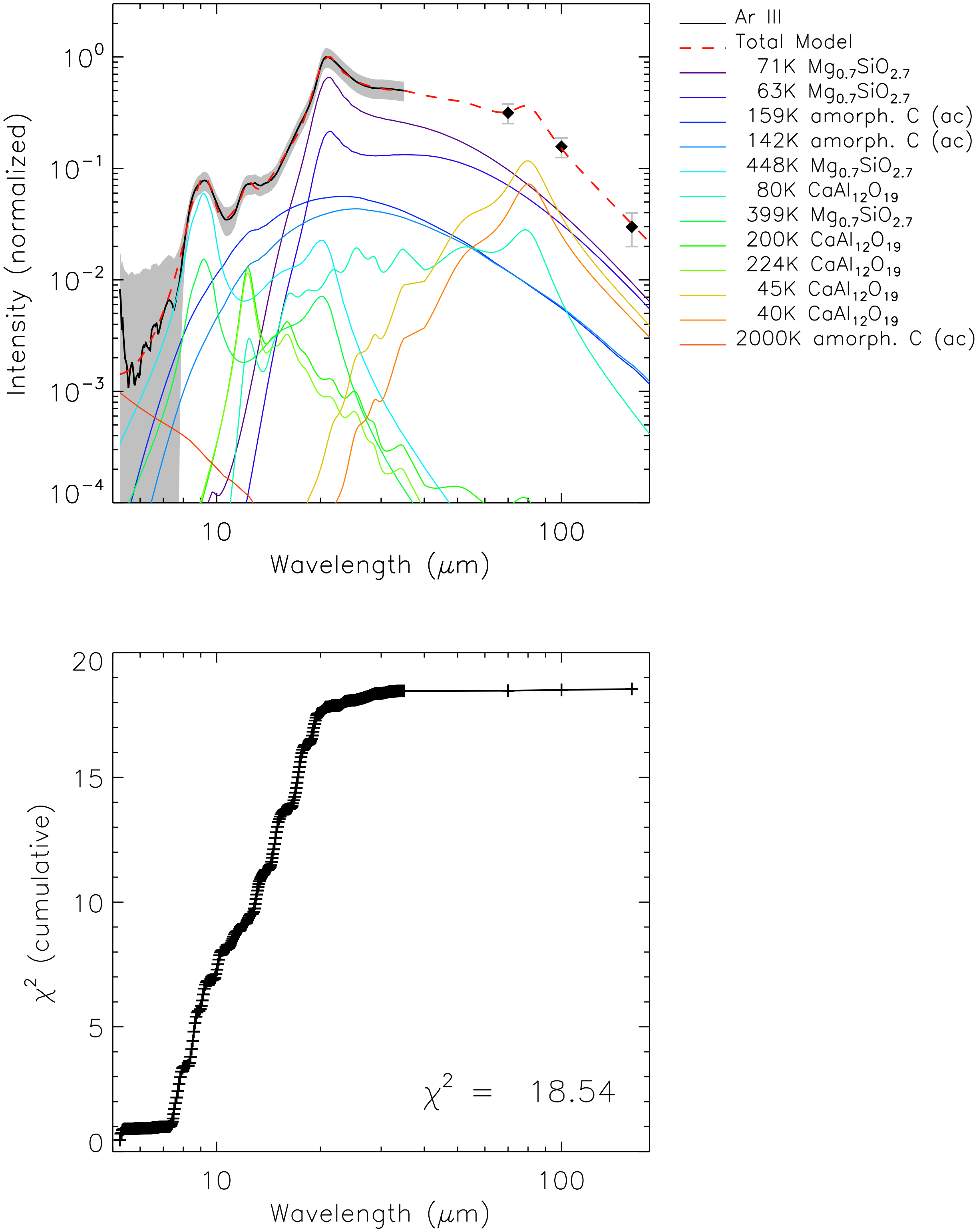

Fig. 21.— The best 3-component fit to the Ar III spectrum uses $CaAl_{12}O_{19}$ (hibonite) to fit the 12 μm peak.

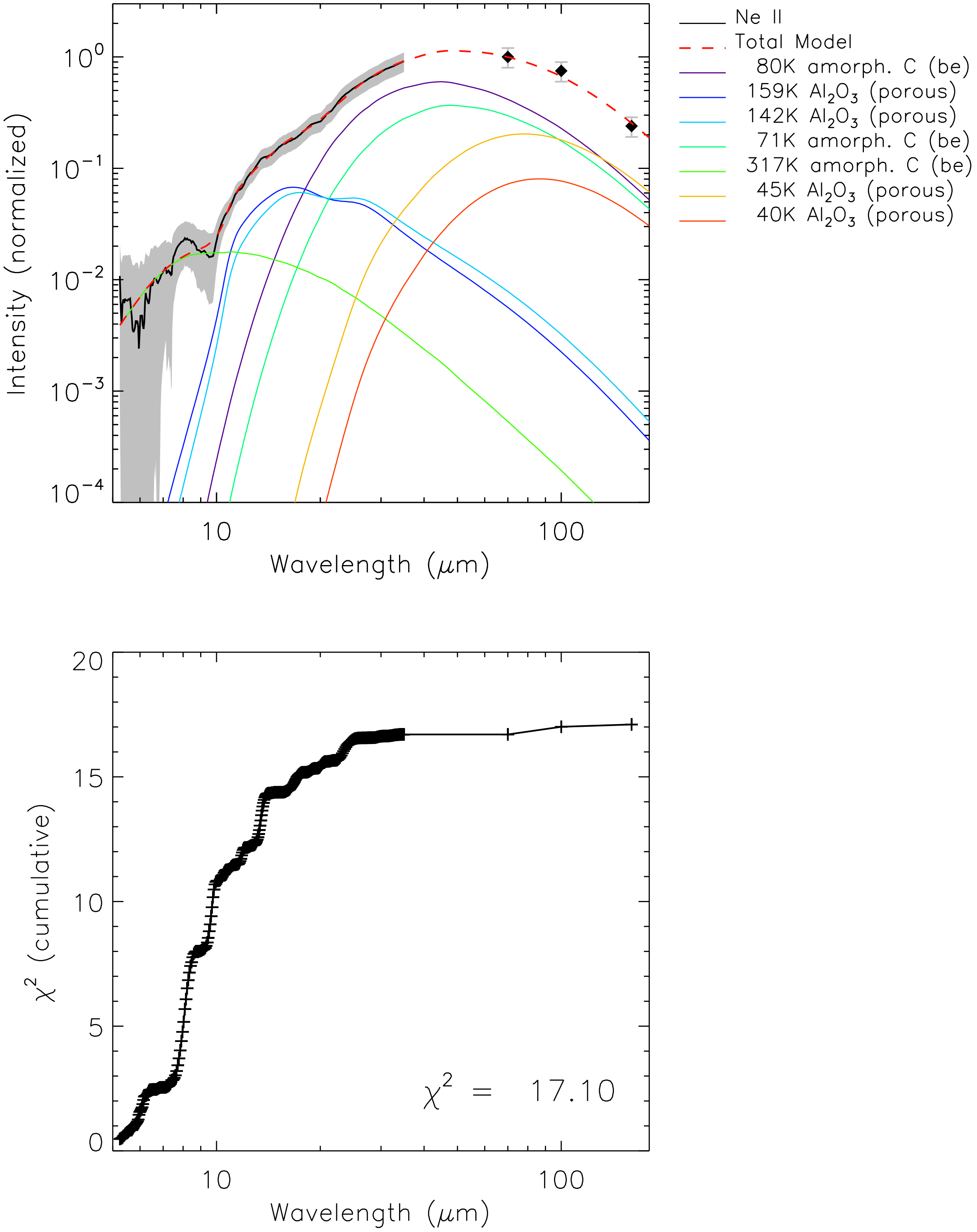

Fig. 22.— The best 2-component fits to the Ne II spectrum use Al_2O_3 in combination with a more featureless component. No silicates are a good match for this very smooth spectrum.

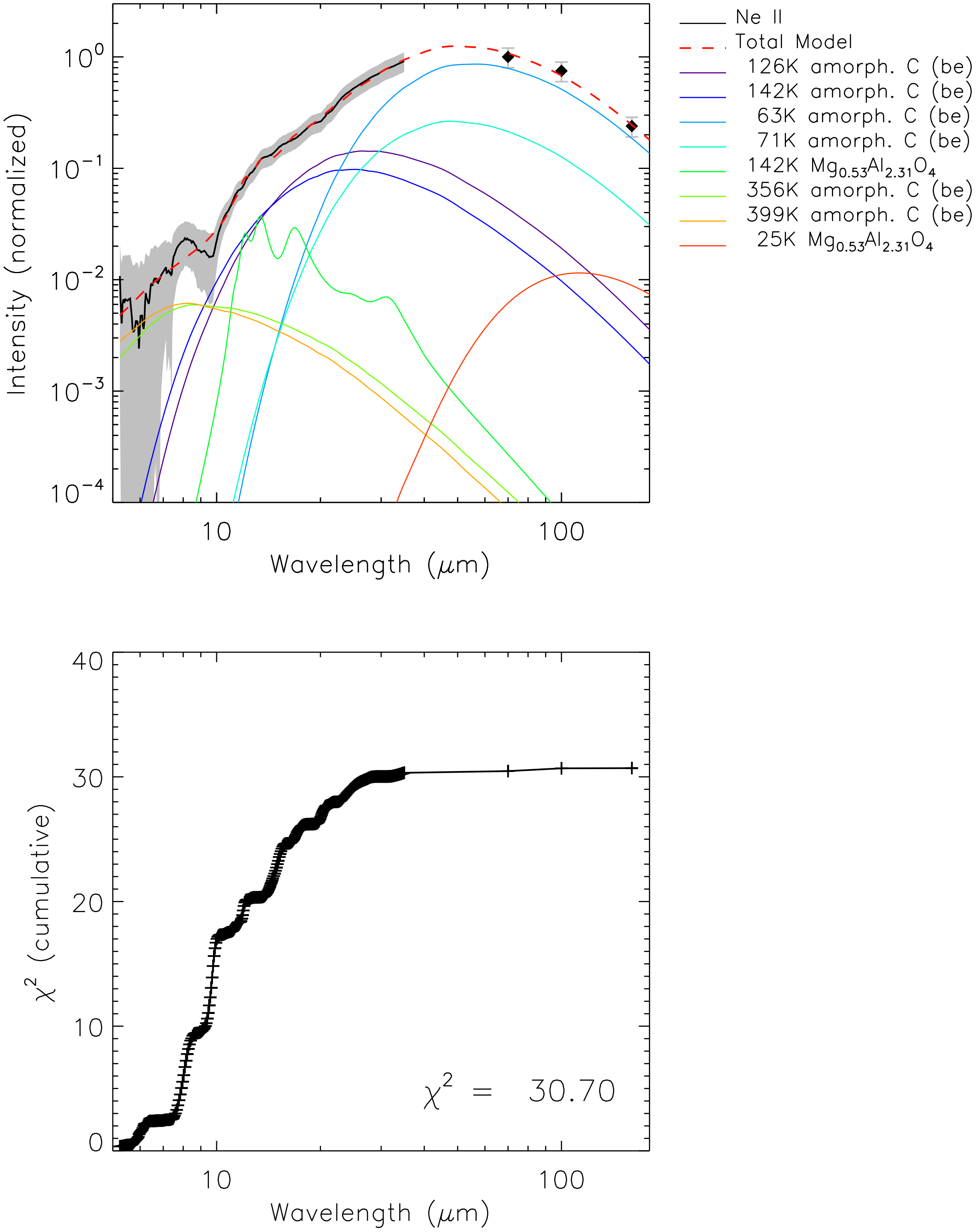

Fig. 23.— An alternate 2-component fit to the Ne II spectrum can be found using nonstoichiometric spinel instead of Al_2O_3.

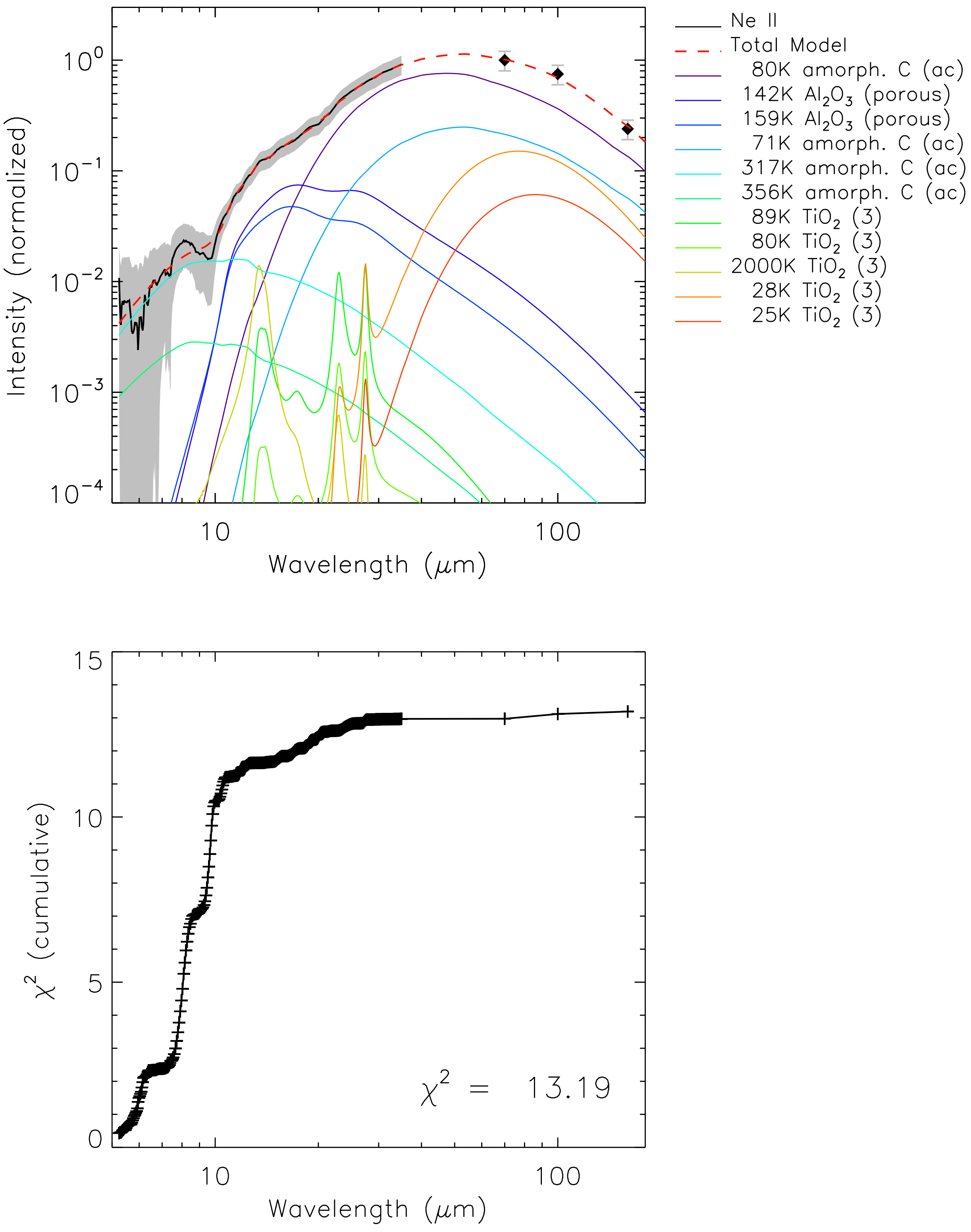

Fig. 24.— The best 3-component fit to the Ne II spectrum adds TiO_2, but the improvement in the fit is very small.

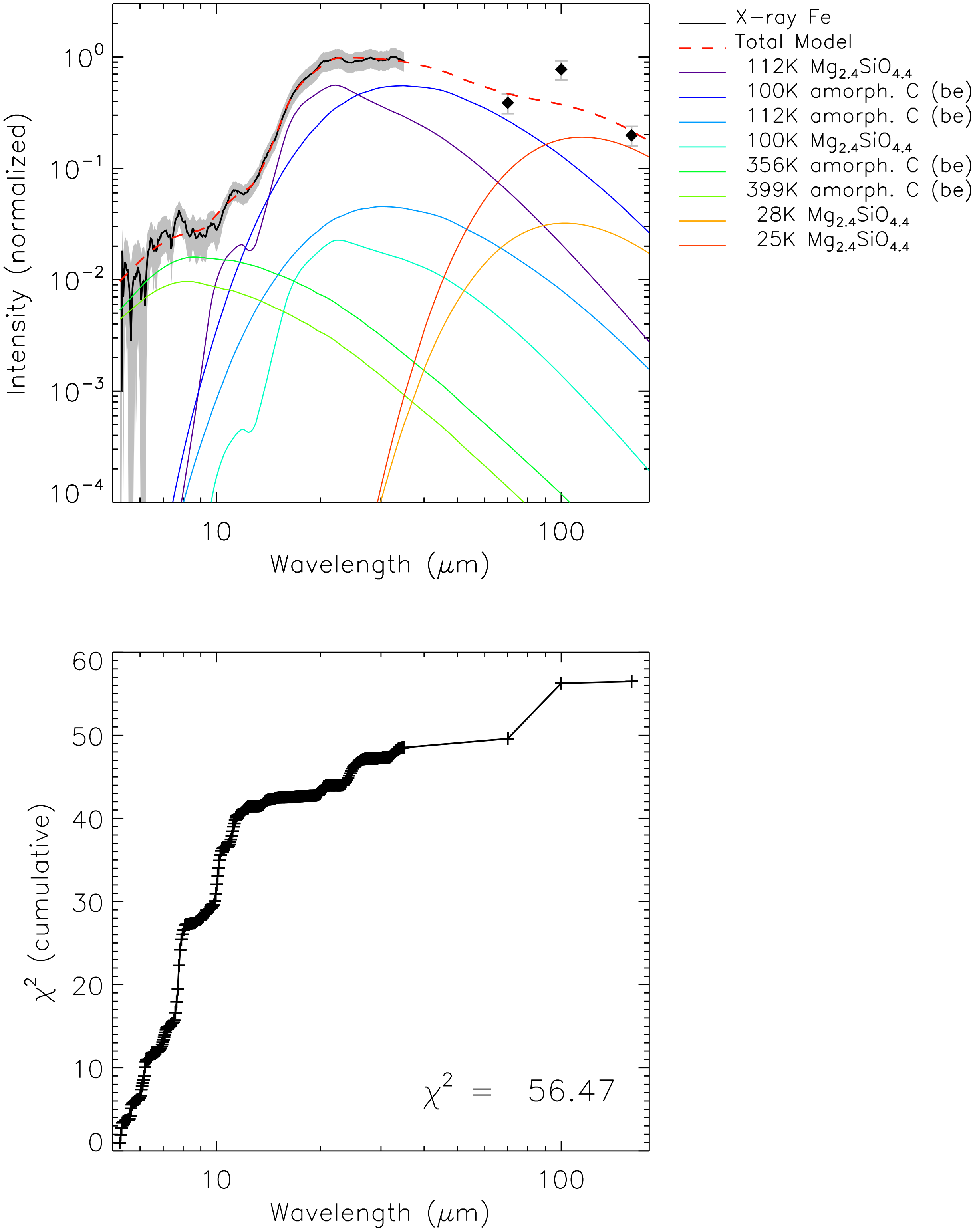

Fig. 25.— The best 2-component fit to the X-ray Fe spectrum uses a Mg silicate in combination with a featureless composition.

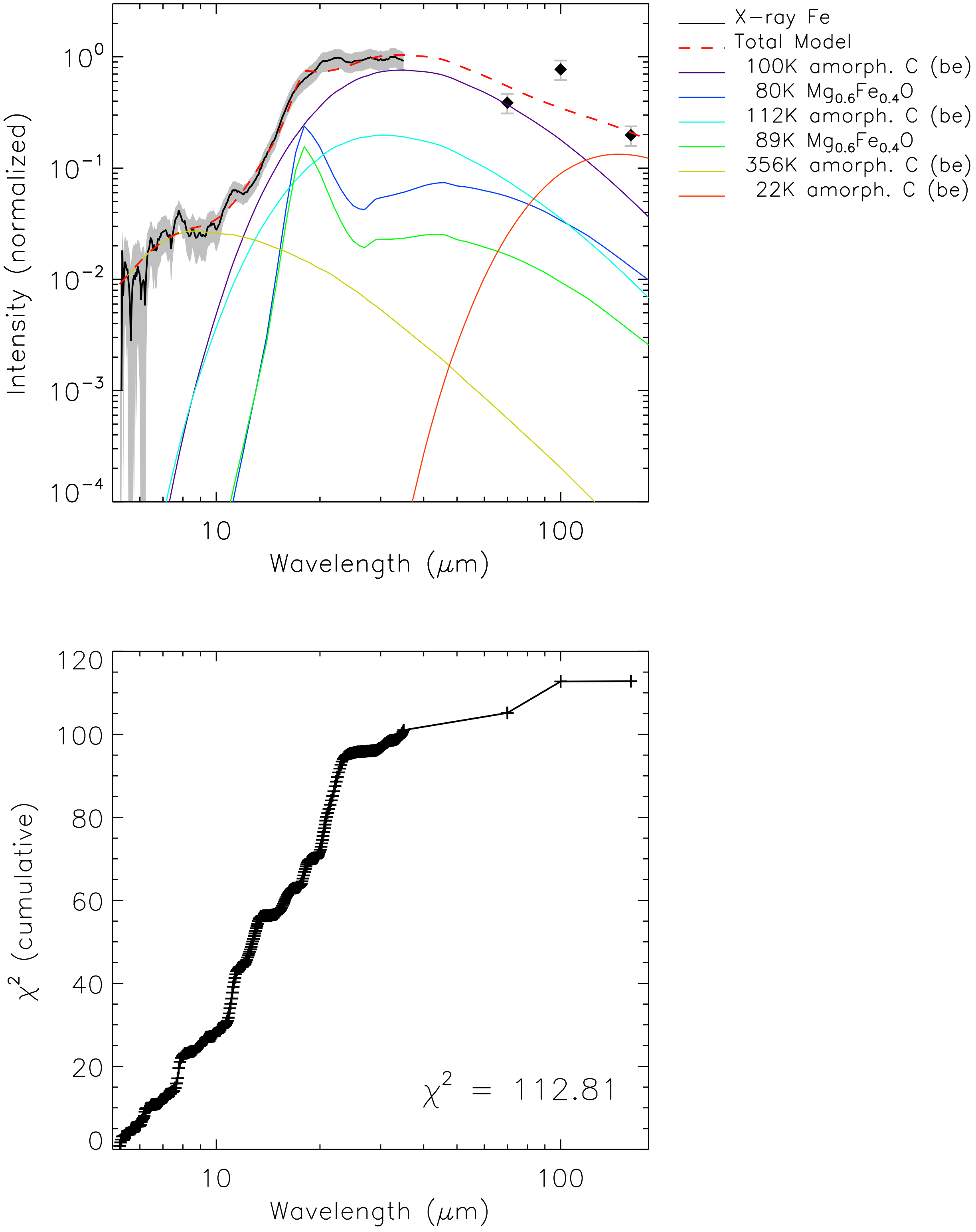

Fig. 26.— This alternate 2-component fit (without silicates) to the X-ray Fe spectrum is about a factor of 2 worse than the best fit, and is thus only marginally acceptable.

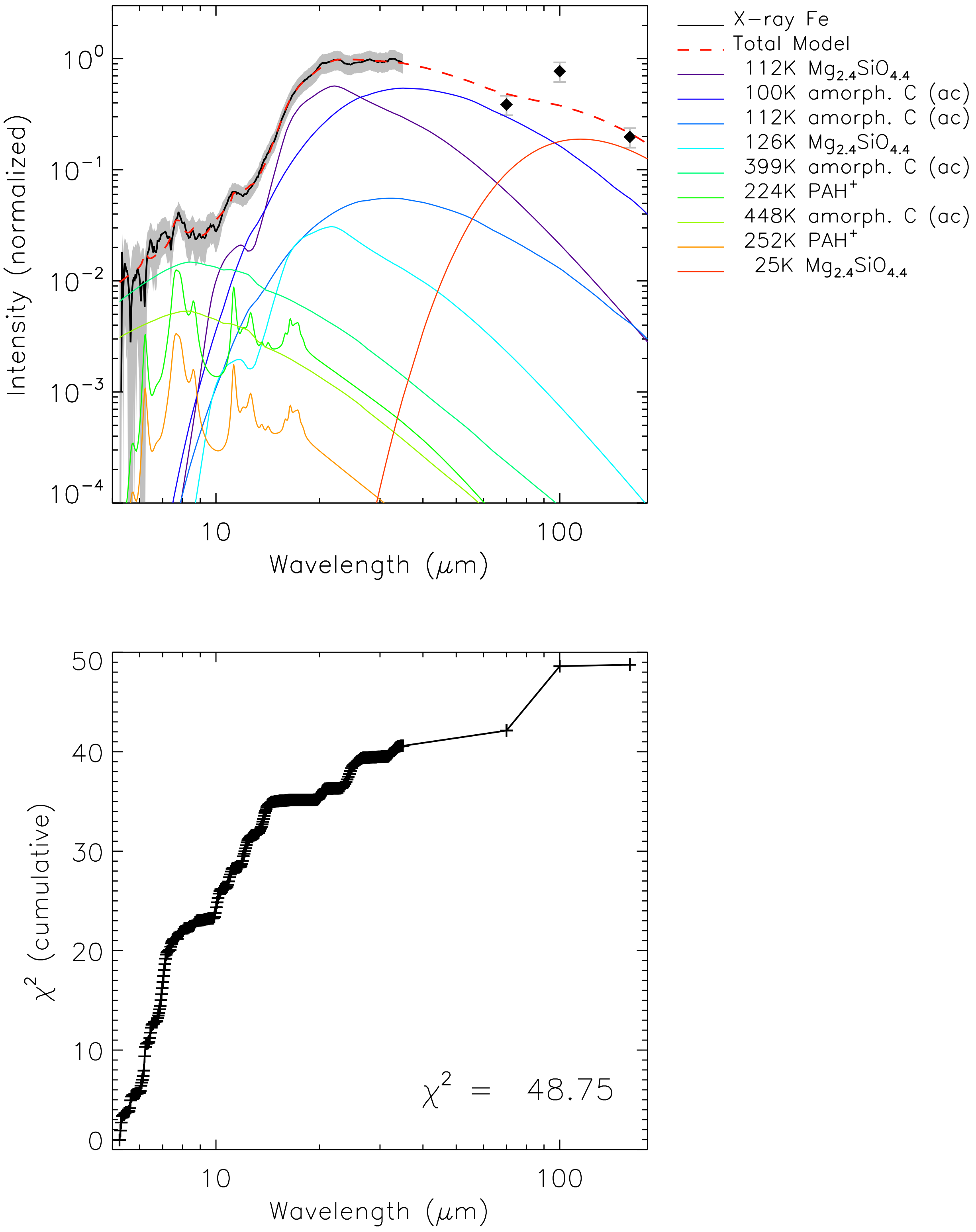

Fig. 27.— The best 3-component fit to the X-ray Fe spectrum uses ionized PAHs to match the small (and possibly spurious) bump at 8 μm.

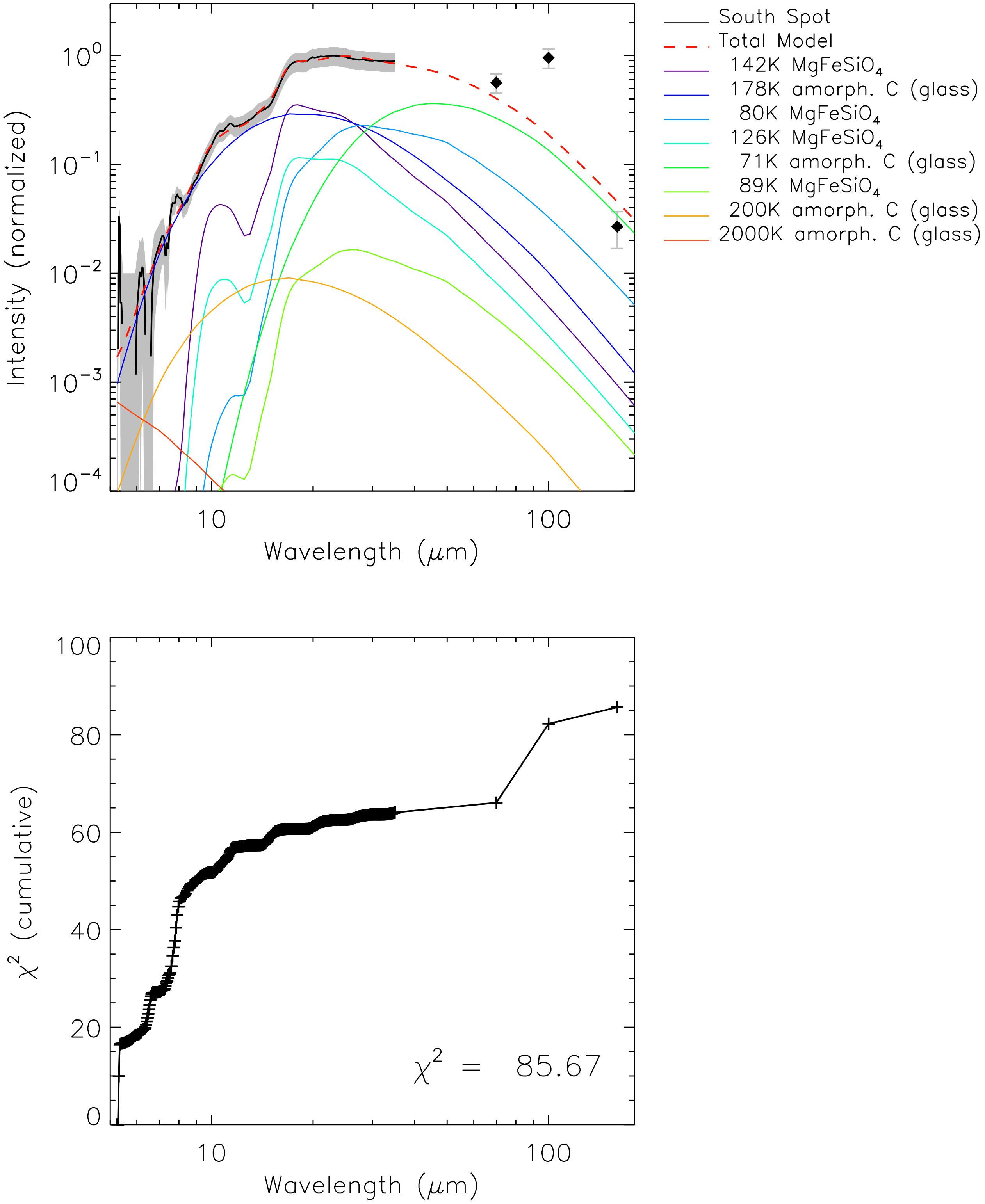

Fig. 28.— The best 2-component fits to the South Spot spectrum are similar to those for the X-ray Fe spectrum, but involved higher dust temperatures for the dominant components.

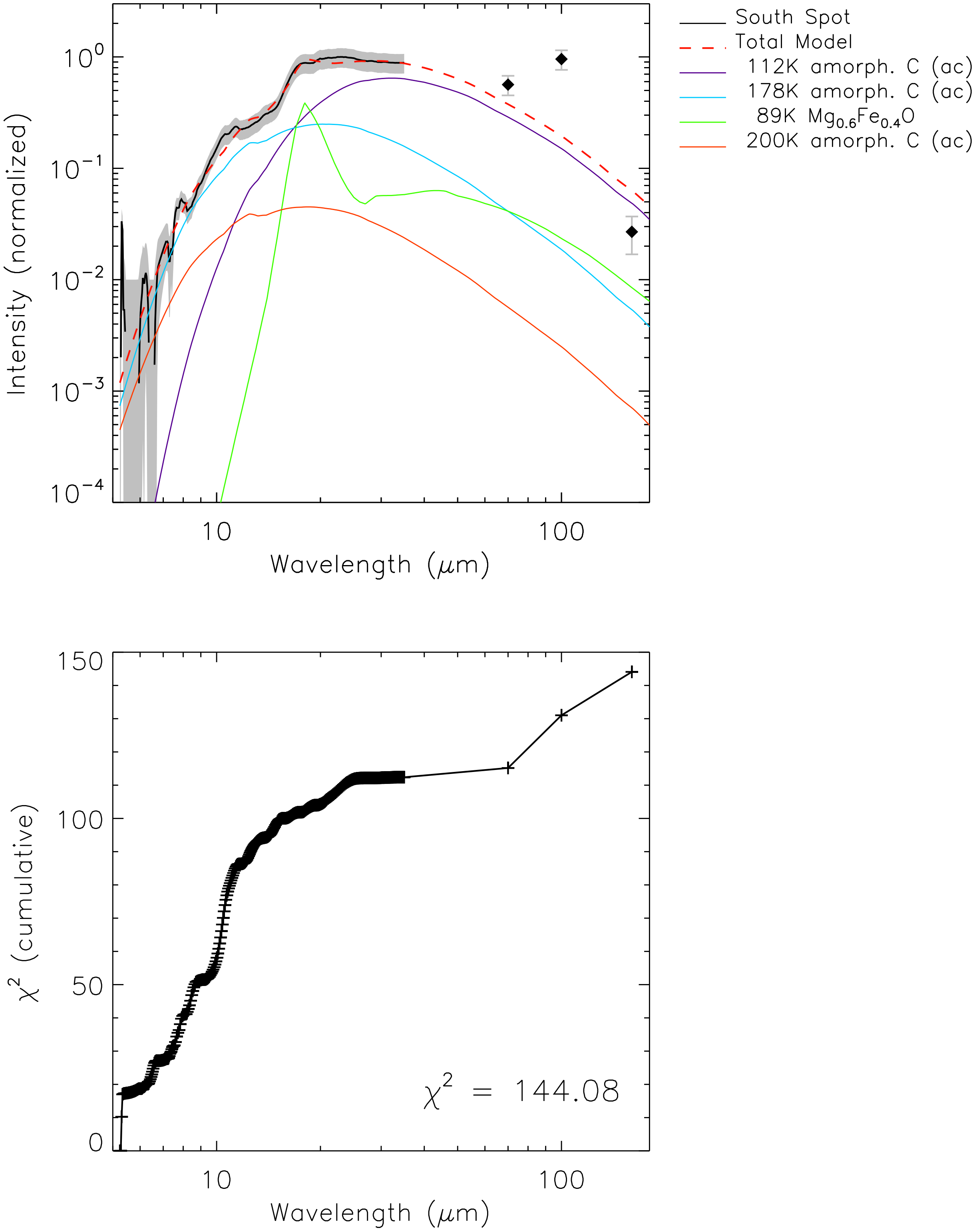

Fig. 29.— An alternate 2-component fit to the South Spot spectrum again shows that reasonable (though worse) fits can also be obtained without the use of silicates.

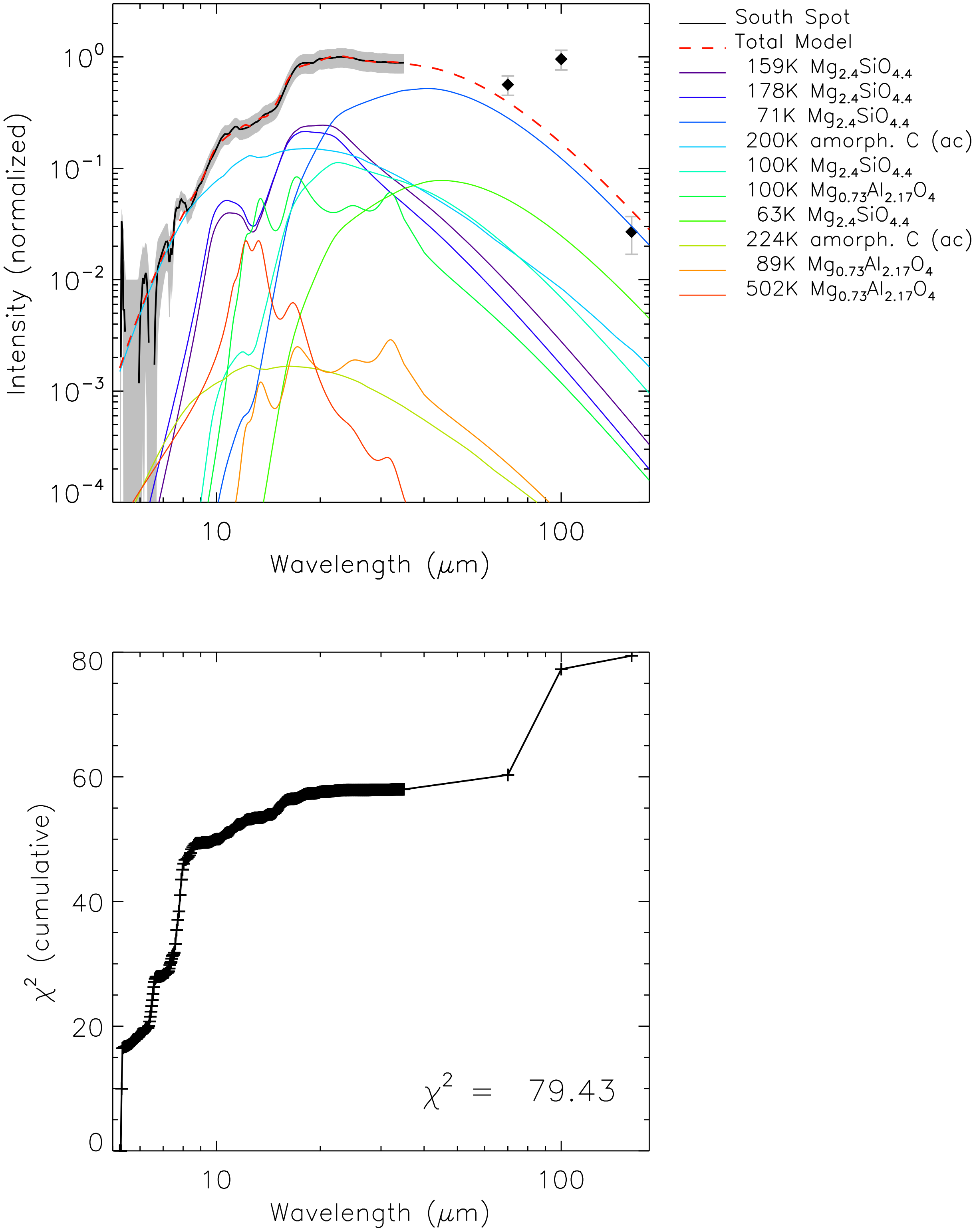

Fig. 30.— The best 3-component fit to the South Spot spectrum uses nonstoichiometric spinel as a third component to make relatively minor adjustments to the model.

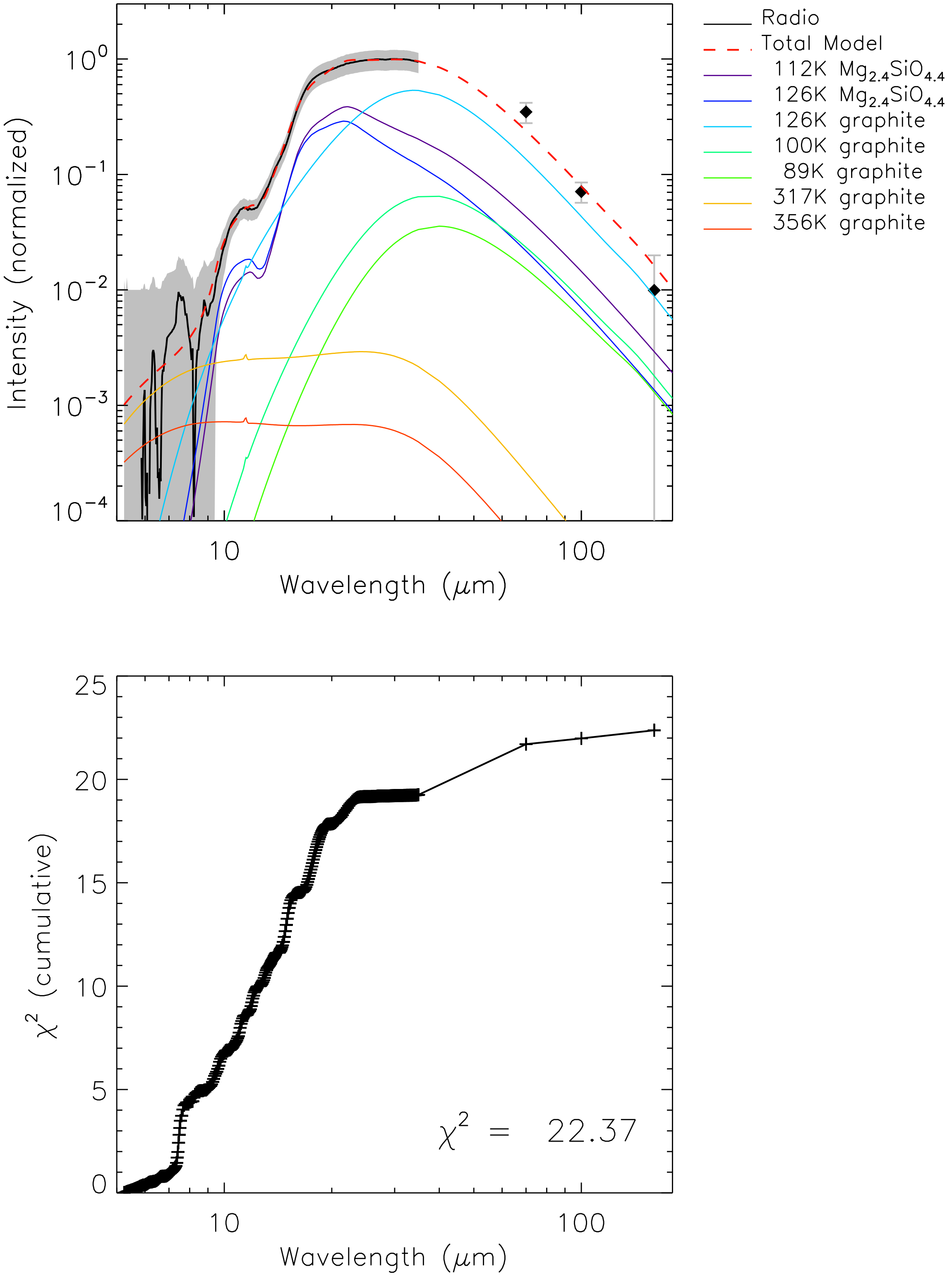

Fig. 31.— The best 2-component fit to the Radio spectrum uses graphite and a Mg silicate. Combinations of other silicates with other featureless components are nearly as good.

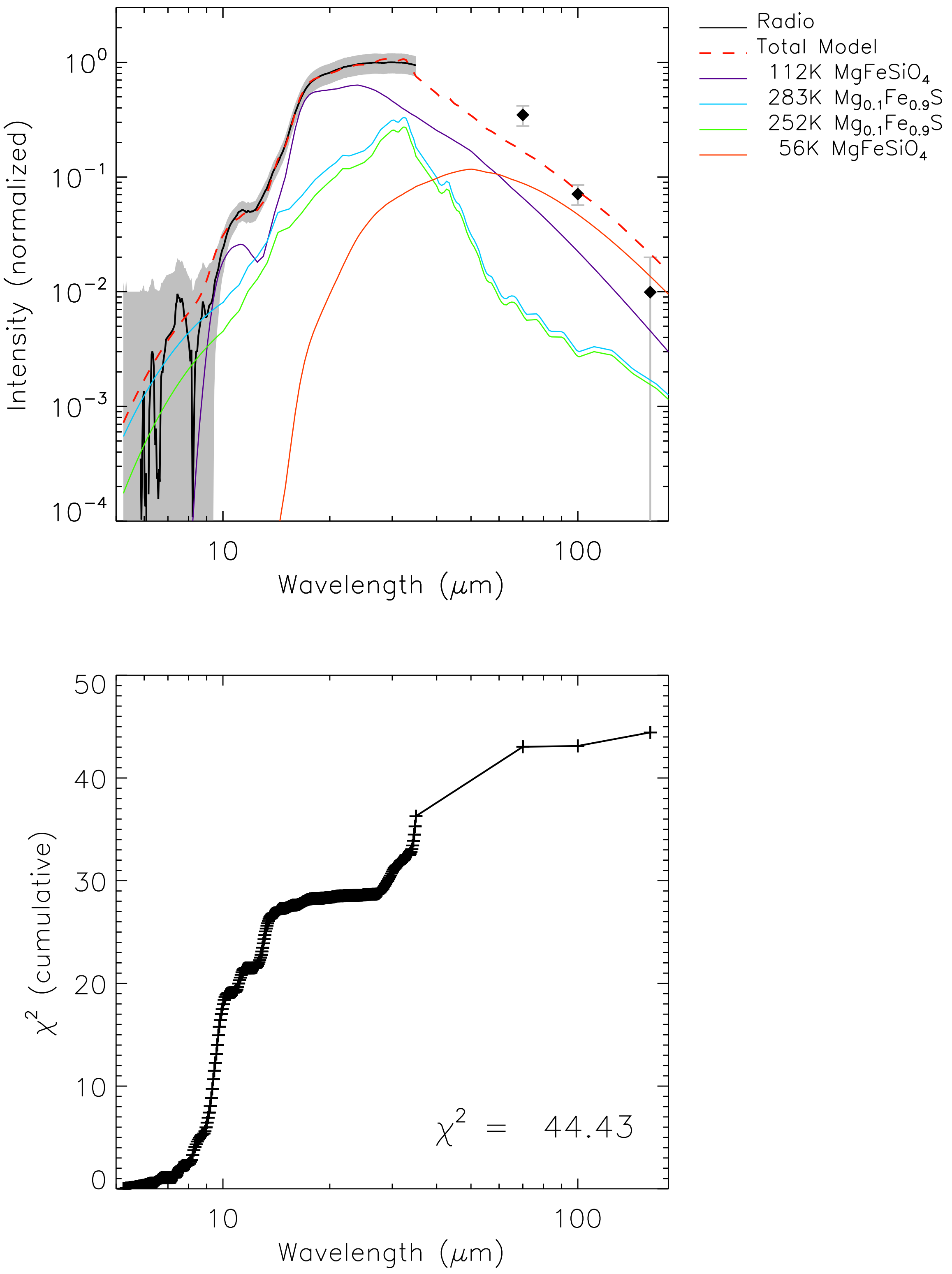

Fig. 32.— This alternate fit to the Radio spectrum shows a marginal model using a sulfide composition instead of a one of the more featureless dust compositions.

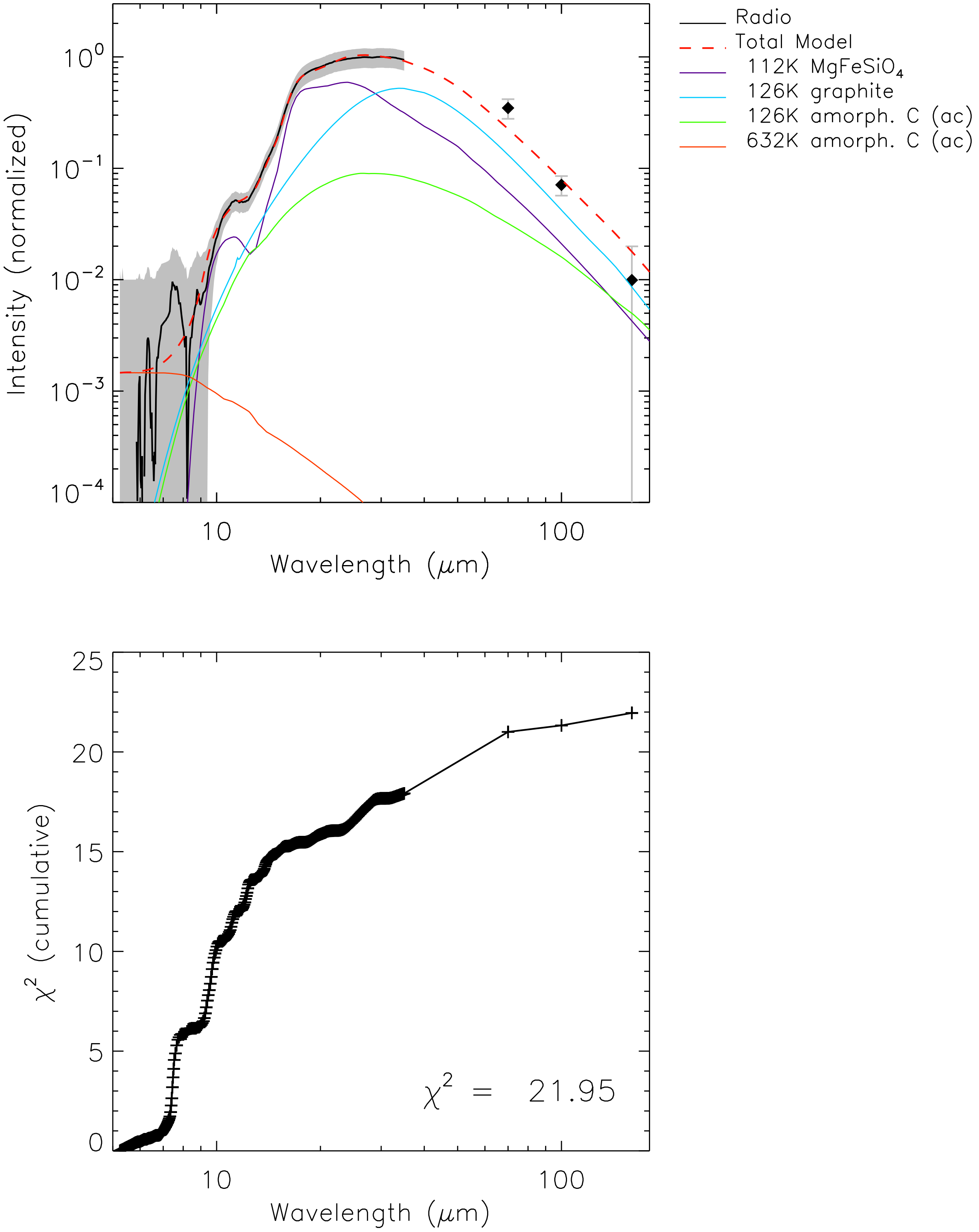

Fig. 33.— The best 3-component fit to the Radio spectrum is only very slightly better than the 2-component fit.

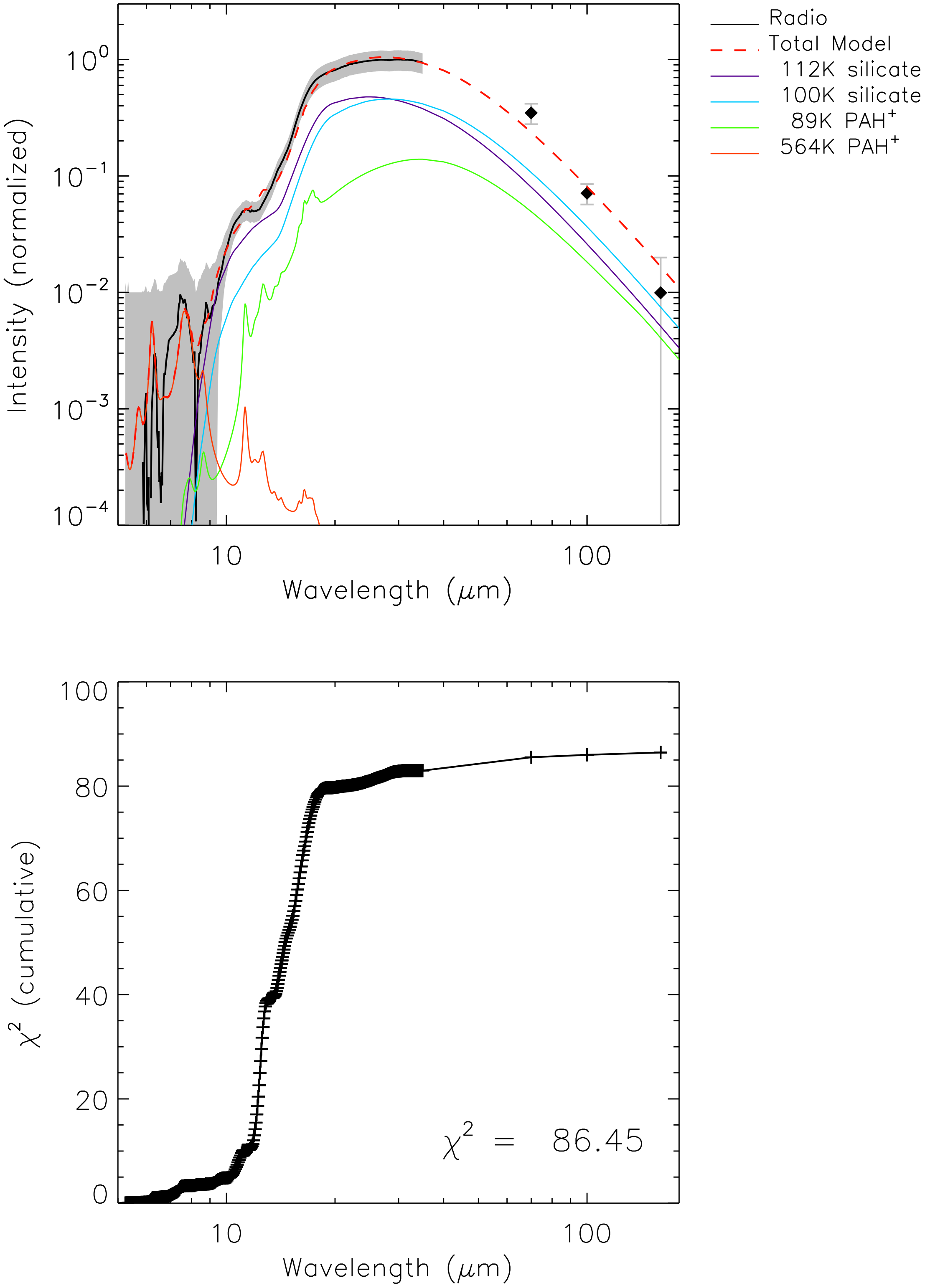

Fig. 34.— The fit of the Radio spectrum using the standard astronomical silicate, graphite, PAH, and PAH$^+$ combination. Only two of the four components are actually needed for the fit since the PAH$^+$ component is sufficient to provide a relatively featureless component at $\gtrsim 20$ μm and the PAH emission band at ~ 8 μm.

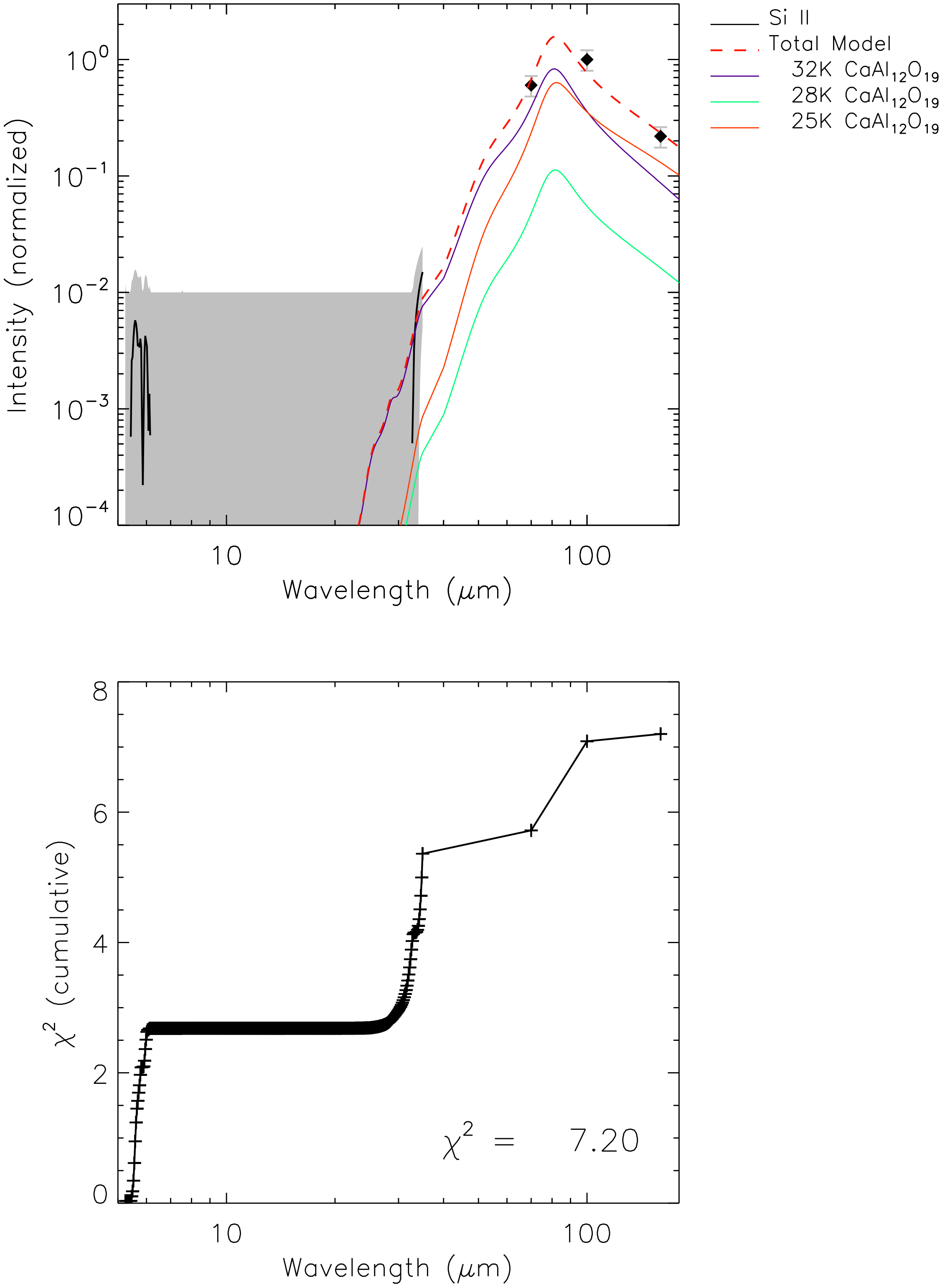

Fig. 35.— The best 1-component fit to the Si II spectrum uses $CaAl_{12}O_{19}$, which happens to have a broad peak in its emissivity at ∼ 80 μm

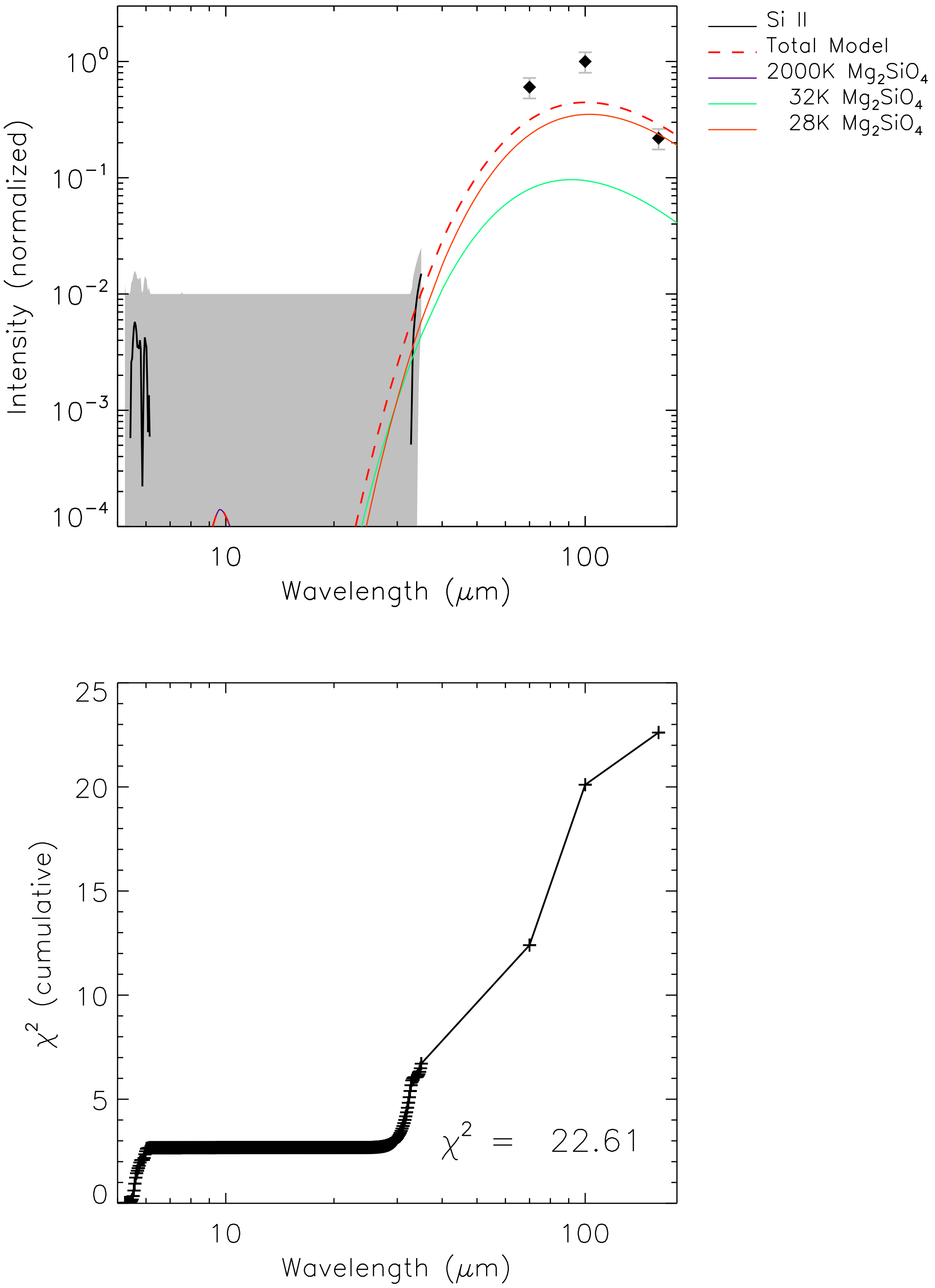

Fig. 36.— This alternate fit to the Si II spectrum uses Mg_2SiO_4 which has a more typical power law emissivity with an index of −2 at long wavelengths.

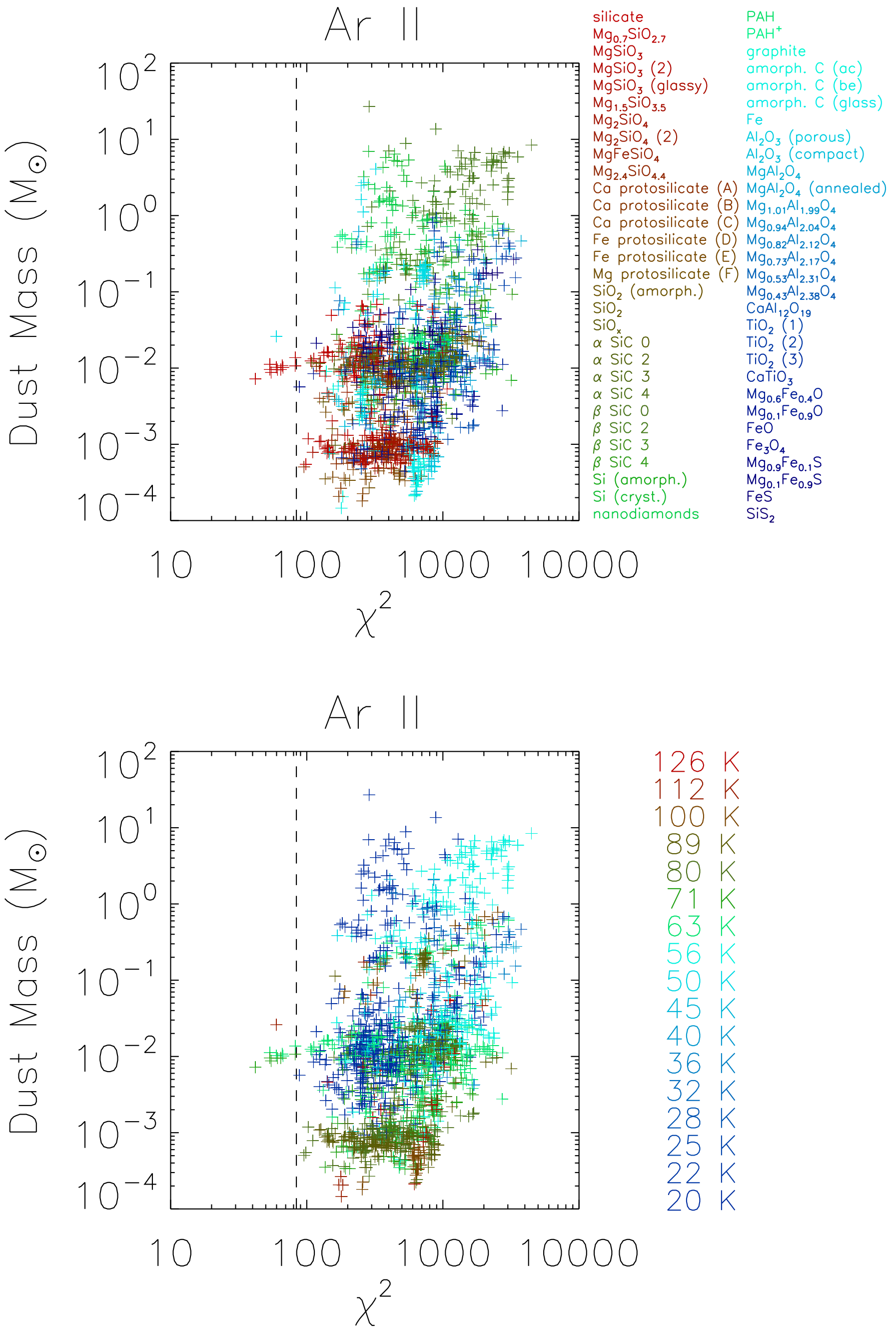

Fig. 37.— Total dust masses for Ar II models. In the top panel the points are color coded by the composition that provides the largest mass component. In the bottom panel the masses are color coded by the temperature of the dominant mass component. Only models to the left of the dashed line (within a factor of 2 in χ^2 of the best model) are deemed acceptable. These good models indicate that $\sim 10^{-2}$ M$_\odot$ of dust, mostly silicates at $\sim$ 70K is associated with the Ar II emission in Cas A.

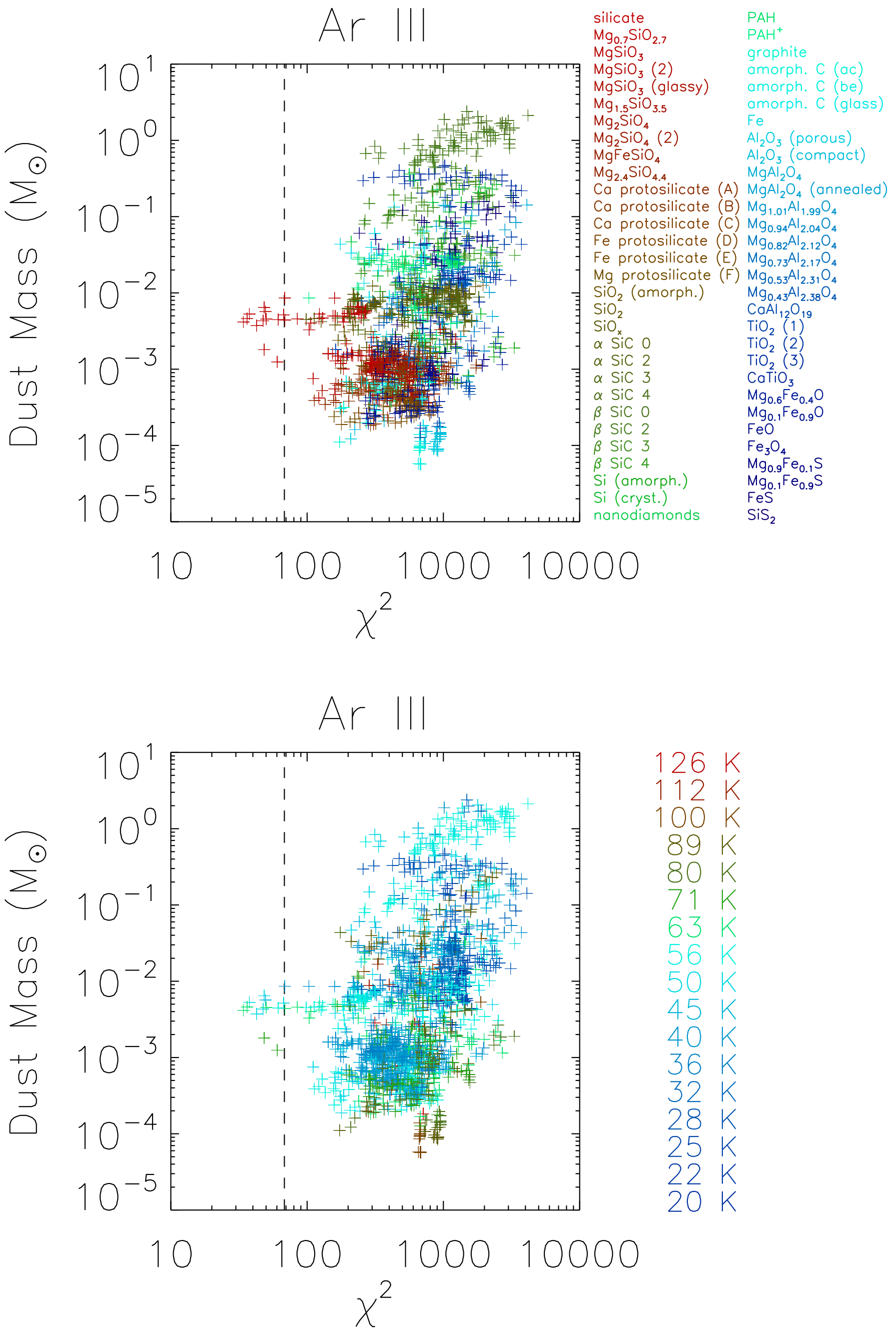

Fig. 38.— Total dust masses associated with Ar III emission. Results are similar to the models for Ar II, but the total mass is only half as large.

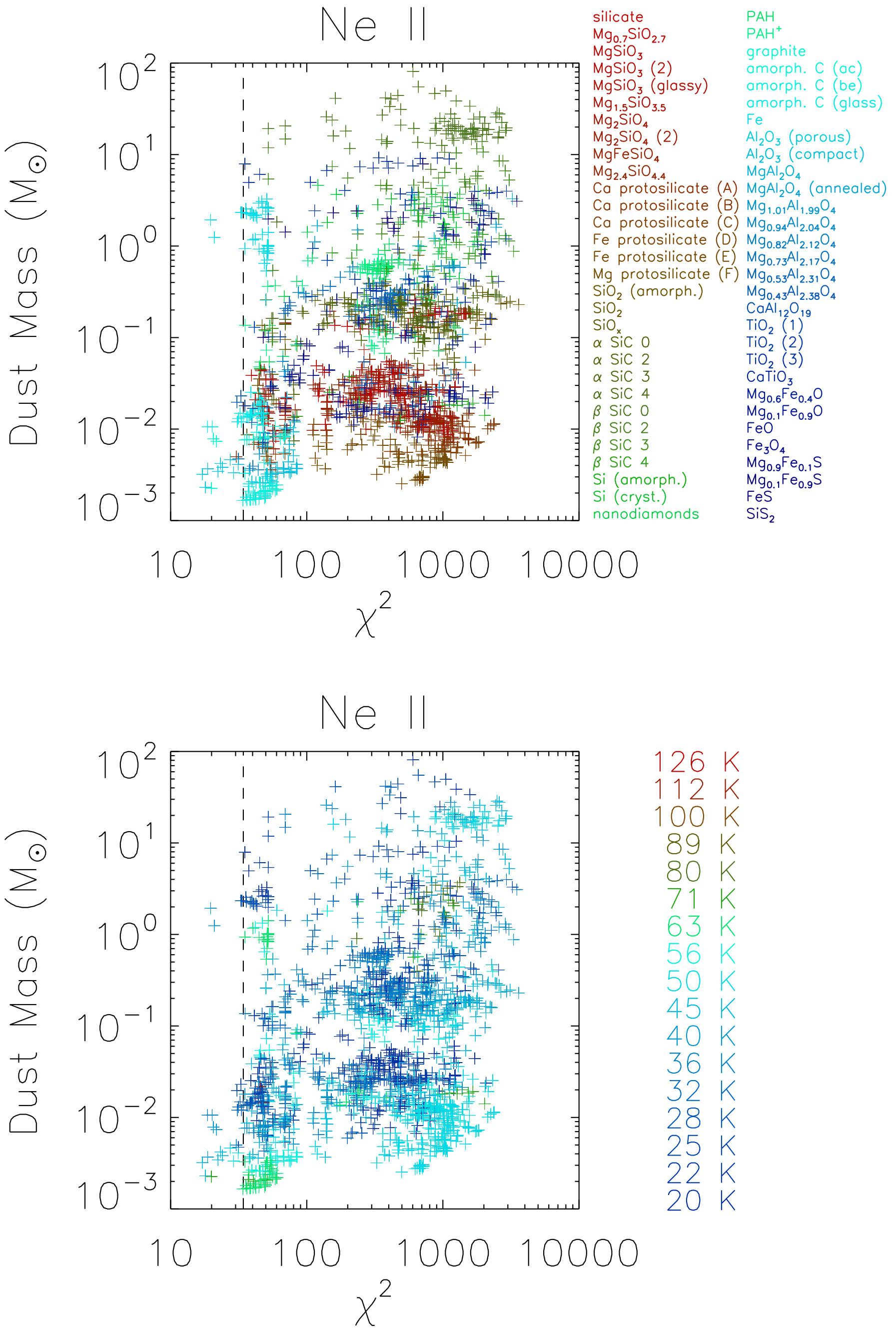

Fig. 39.— Total dust masses associated with the Ne II emission. Here the mass is dominated by one of the more featureless compositions or Al_2O_3, and the derived total mass depends on the long wavelength emissivity for the dominant component. The good models with total masses > 1 $M_\odot$ are dominated by Fe dust which has a very low long wavelength emissivity, and thus requires extreme dust masses to produce the observed emission.

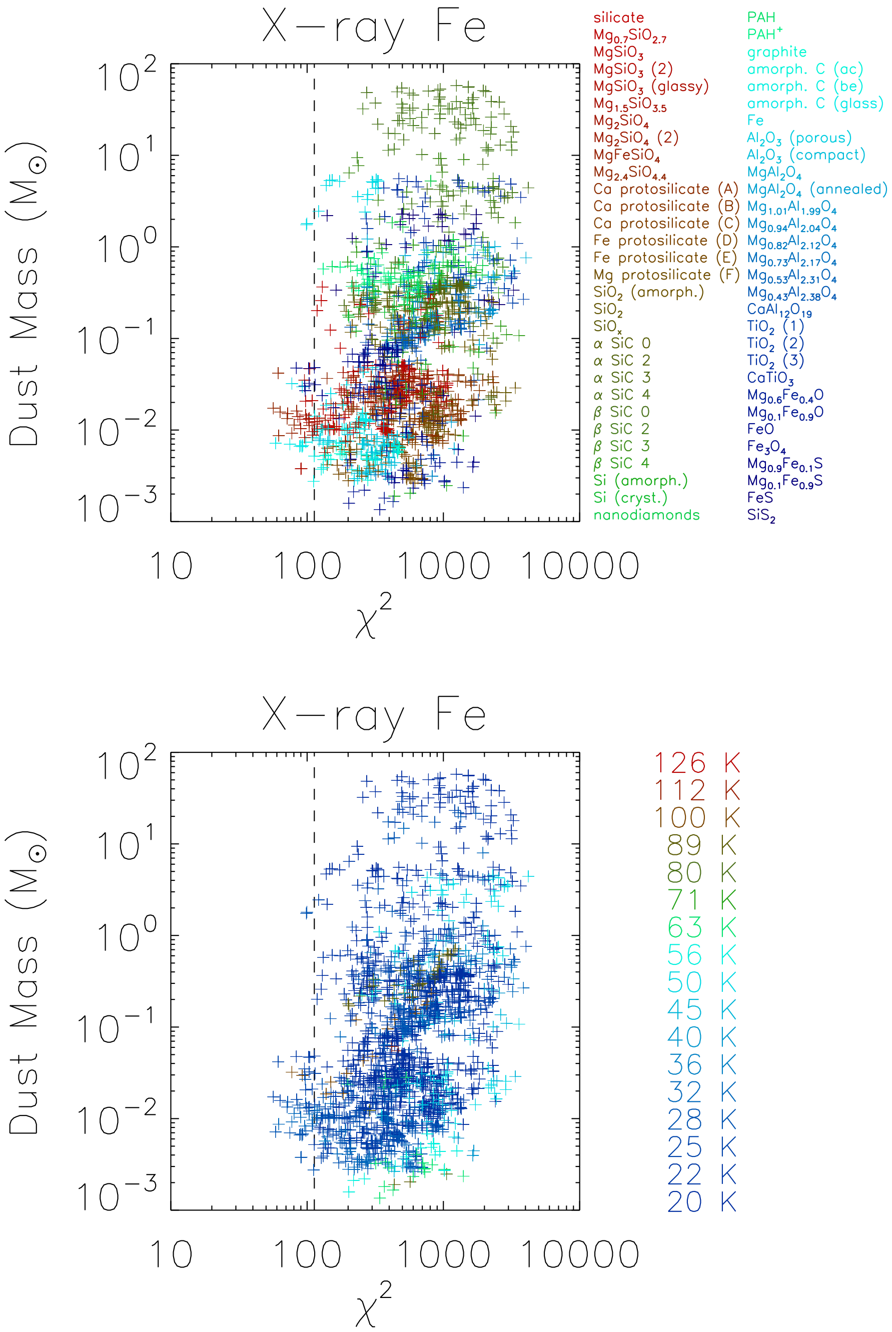

Fig. 40.— Total dust masses associated with X-ray Fe emission. Among the good models, the range in mass is caused by the variation in long wavelength emissivity between different dominant compositions.

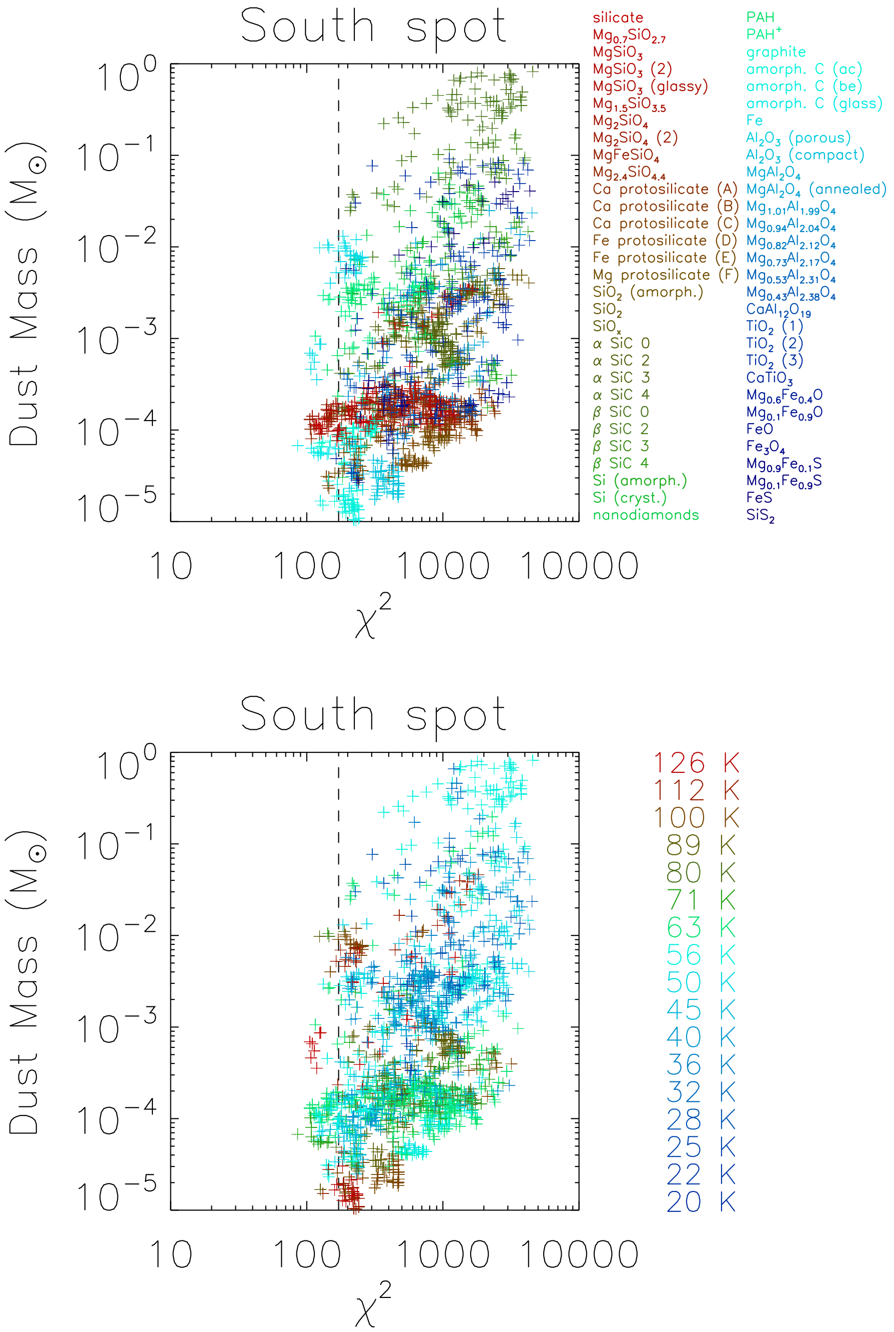

Fig. 41.— Total dust masses associated with the South Spot emission. As indicated in Fig. 11, there are many different possible compositions that can yield good fits to this spectrum. Thus there is a wide spread in mass, depending on what composition is dominant.

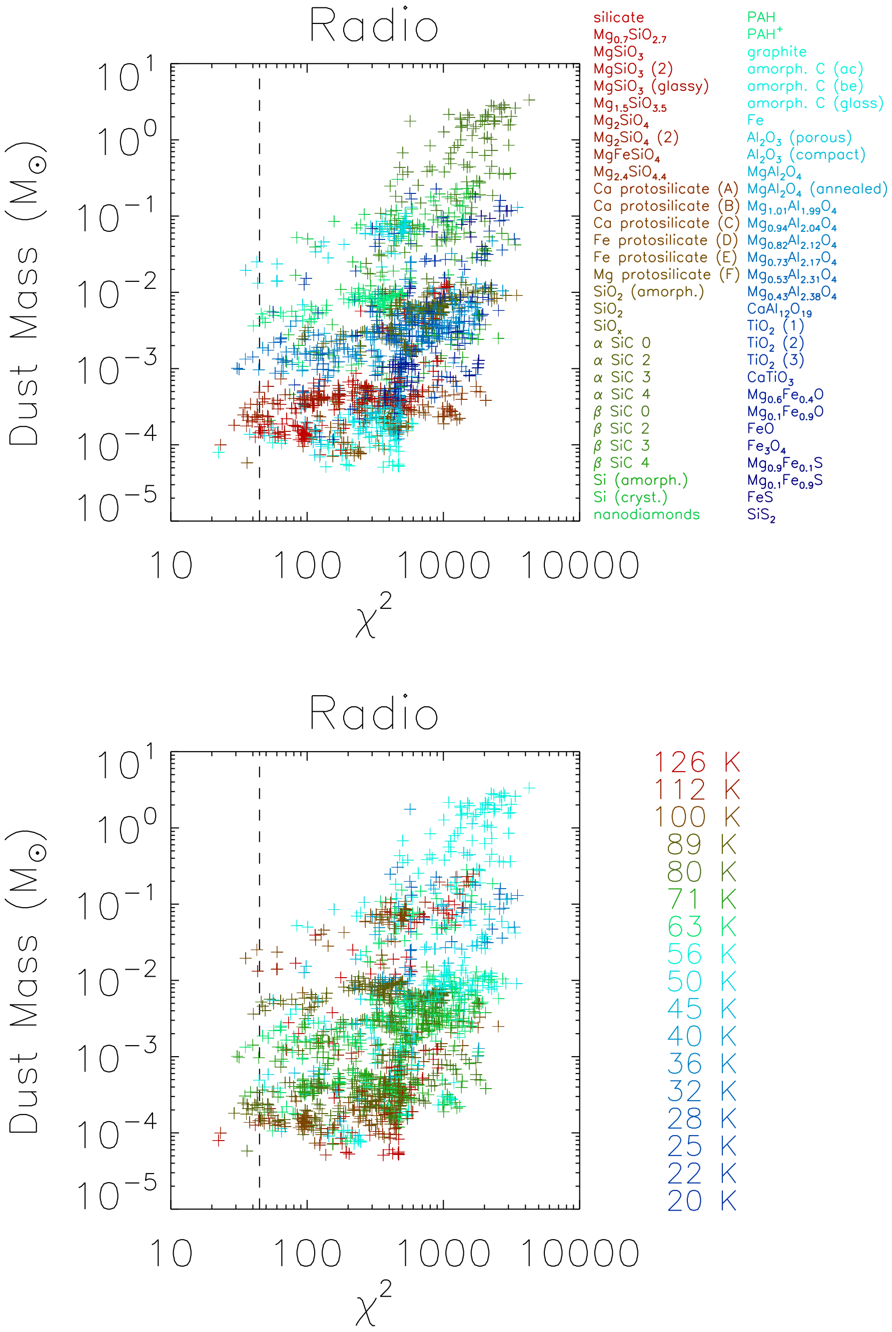

Fig. 42.— Total dust mass associated with the Radio emission. Again for the best models, there is a relatively broad range in mass that is dependent on the composition of the dominant component.

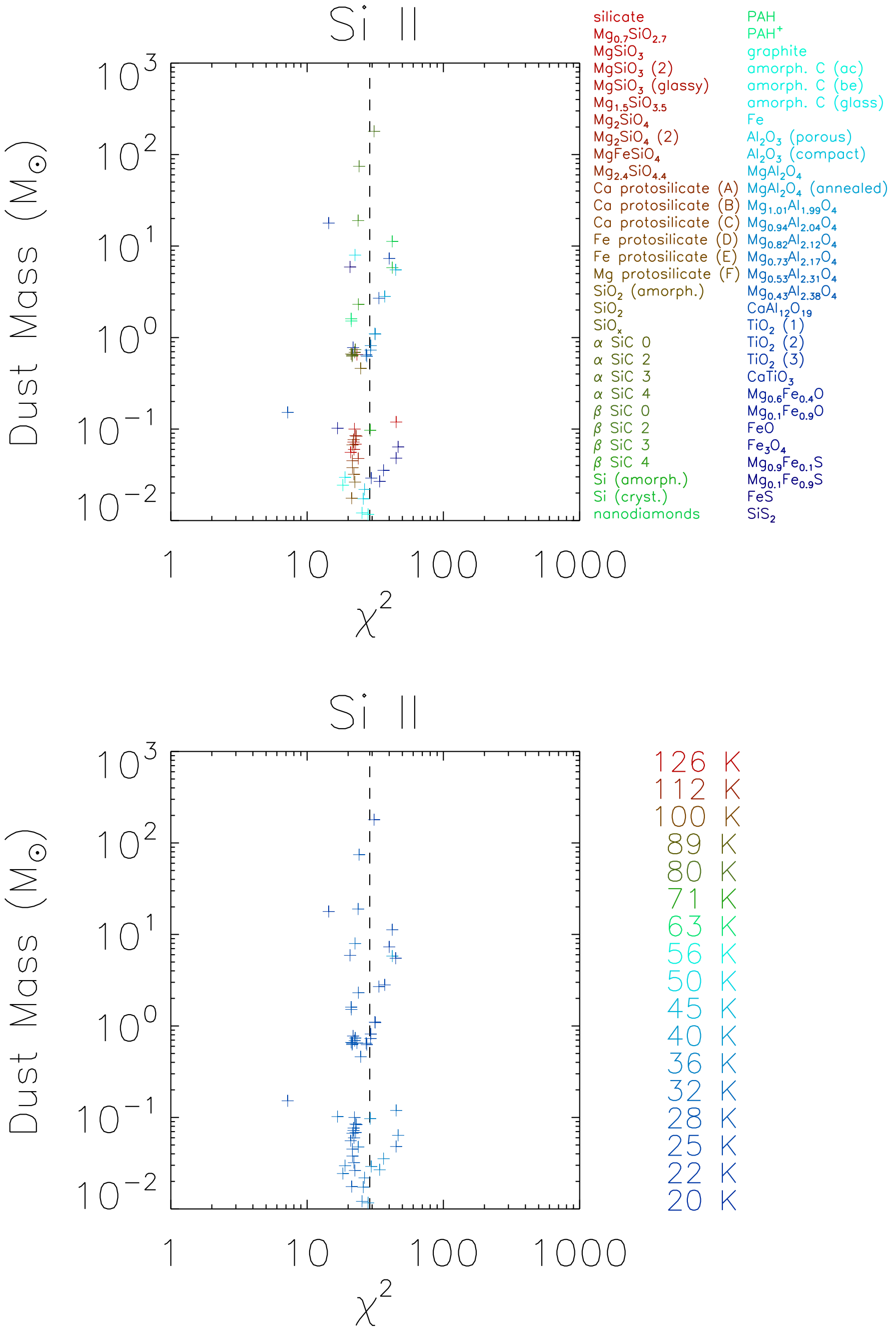

Fig. 43.— Total dust mass associated with the Si II emission. Here models within a factor of 4 of the minimum χ^2 are deemed acceptable, rather than the factor of 2 used in other cases. This is because the limited data appear to have underestimated uncertainties and have a coincidentally good fit to one dust composition ($CaAl_{12}O_{19}$) that has a sharp feature at ∼80 μm. While all compositions must be cold to fit the data, the composition itself, and thus the mass, is not well constrained.

Table 1. Linear Correlation Coefficients between the Spatial Templates

	[Ar II]	**[Ar III]**	[S IV]	[Ne V]	[Fe II]	[S III]	IRAC 8 μm	**[Ne II]**	[Ne III]	IRAC 4.5 μm	[O IV]+[Fe II]	[S III]	**[Si II]**	**X-ray Fe**	X-ray Si	**Radio**
[Ar II] 6.99 μm	1.00	0.99	0.97	0.89	0.77	0.97	0.97	0.76	0.76	0.88	0.83	0.84	0.54	0.44	0.67	0.54
[Ar III] 8.99 μm	···	1.00	0.97	0.88	0.78	0.95	0.97	0.73	0.73	0.87	0.82	0.83	0.56	0.46	0.68	0.54
[S IV] 10.51 μm	···	···	1.00	0.85	0.74	0.96	0.93	0.74	0.75	0.84	0.88	0.89	0.66	0.41	0.65	0.55
[Ne V] 14.32 μm	···	···	···	1.00	0.73	0.90	0.85	0.78	0.81	0.84	0.82	0.82	0.56	0.45	0.65	0.53
[Fe II] 17.94 μm	···	···	···	···	1.00	0.74	0.76	0.58	0.61	0.73	0.67	0.65	0.45	0.34	0.48	0.45
[S III] 18.71 μm	···	···	···	···	···	1.00	0.92	0.77	0.79	0.85	0.88	0.90	0.64	0.46	0.70	0.58
IRAC 8 μm	···	···	···	···	···	···	1.00	0.70	0.70	0.87	0.75	0.76	0.45	0.43	0.63	0.47
[Ne II] 12.81 μm	···	···	···	···	···	···	···	1.00	0.96	0.90	0.81	0.73	0.50	0.37	0.50	0.48
[Ne III] 15.56 μm	···	···	···	···	···	···	···	···	1.00	0.88	0.83	0.75	0.54	0.42	0.52	0.50
IRAC 4.5 μm	···	···	···	···	···	···	···	···	···	1.00	0.81	0.76	0.49	0.45	0.58	0.54
[O IV]+[Fe II] 26 μm	···	···	···	···	···	···	···	···	···	···	1.00	0.93	0.83	0.39	0.64	0.62
[S III] 33.48 μm	···	···	···	···	···	···	···	···	···	···	···	1.00	0.84	0.41	0.62	0.62
[Si II] 34.82 μm	···	···	···	···	···	···	···	···	···	···	···	···	1.00	0.23	0.42	0.55
X-ray Fe	···	···	···	···	···	···	···	···	···	···	···	···	···	1.00	0.71	0.65
X-ray Si	···	···	···	···	···	···	···	···	···	···	···	···	···	···	1.00	0.75
Radio	···	···	···	···	···	···	···	···	···	···	···	···	···	···	···	1.00

Note. — Spatial templates in boldface were selected as the basis for further analysis.

Table 2. Dust Emissivities

n	Composition	λ Range (μm)	Note	Reference
Silicates				
0	Silicate	0.01–9400		Draine & Lee (1984)
1	$Mg_{0.7}SiO_{2.7}$	0.2–470		Jäger et al. (2003)
2	$MgSiO_3$	0.2–10000		Jäger et al. (2003)
3	$MgSiO_3$	0.1–100000		Kozasa
4	$MgSiO_3$	0.2–500	glassy	Jäger et al. (1994); Dorschner et al. (1995)
5	$Mg_{1.5}SiO_{3.5}$	0.2–6000		Jäger et al. (2003)
6	Mg_2SiO_4	0.2–950		Jäger et al. (2003)
7	Mg_2SiO_4	0.1–100000		Kozasa
8	$MgFeSiO_4$	0.2–500	glassy	Jäger et al. (1994); Dorschner et al. (1995)
9	$Mg_{2.4}SiO_{4.4}$	0.2–8200		Jäger et al. (2003)
Protosilicates				
10	Ca Protosilicate	7.6–25	A – unheated	Dorschner et al. (1980)
11	Ca Protosilicate	7.7–25	B – 450C	Dorschner et al. (1980)
12	Ca Protosilicate	7.8–25	C – 695C	Dorschner et al. (1980)
13	Fe Protosilicate	8.2–40	D – unheated	Dorschner et al. (1980)
14	Fe Protosilicate	8–40	E – 490C	Dorschner et al. (1980)
15	Mg Protosilicate	8–40	F – 485C	Dorschner et al. (1980)
Silica				
16	SiO_2	0.1–500	am	Kozasa
17	SiO_2	5–500		Philipp (1985)
18	SiO_x	5.6–520	extrap. at $\lambda > 65$ μm	Rinehart et al. (2011)
SiC, Si				
19	α SiC	0.1–1000	21 μm : $Q_{abs}/a = 0$	Jiang et al. (2005)
20	α SiC	0.1–1000	21 μm : $Q_{abs}/a = 100$	Jiang et al. (2005)
21	α SiC	0.1–1000	21 μm : $Q_{abs}/a = 10^3$	Jiang et al. (2005)
22	α SiC	0.1–1000	21 μm : $Q_{abs}/a = 10^4$	Jiang et al. (2005)
23	β SiC	0.1–1000	21 μm : $Q_{abs}/a = 0$	Jiang et al. (2005)
24	β SiC	0.1–1000	21 μm : $Q_{abs}/a = 100$	Jiang et al. (2005)
25	β SiC	0.1–1000	21 μm : $Q_{abs}/a = 10^3$	Jiang et al. (2005)
26	β SiC	0.1–1000	21 μm : $Q_{abs}/a = 10^4$	Jiang et al. (2005)
27	Si	0.02–247.7	am	Kozasa
28	Si	0.07–433.3	cr	Kozasa
C, Fe				
29	Meteoritic Diamond	0.02–110		Braatz et al. (2000); Mutschke et al. (2004)
30	PAH	0.01–9400		Dwek
31	PAH^+	0.01–9400		Dwek
32	Graphite	0.01–9400		Draine & Lee (1984)

Table 2—Continued

n	Composition	λ Range (μm)	Note	Reference
33	Amorphous Carbon	0.01–9400	ac	Dwek
34	Amorphous Carbon	0.01–9400	be	Dwek
35	Carbon	0.1–3000	glass	Kozasa
36	Fe	0.1–100000		Kozasa
Al Oxides				
37	Al_2O_3	7.8–500	porous	Begemann et al. (1997)
38	Al_2O_3	7.8–200	compact	Begemann et al. (1997)
Oxides				
39	$MgAl_2O_4$	2–10000	natural	Fabian et al. (2001)
40	$MgAl_2O_4$	2–6800	natural, annealed	Fabian et al. (2001)
41	$Mg_{1.01}Al_{1.99}O_4$	1.67–6825	nonstoich. spinel	Zeidler et al. (2011)
42	$Mg_{0.94}Al_{2.04}O_4$	1.67–6825	nonstoich. spinel	Zeidler et al. (2011)
43	$Mg_{0.82}Al_{2.12}O_4$	1.67–6825	nonstoich. spinel	Zeidler et al. (2011)
44	$Mg_{0.73}Al_{2.17}O_4$	1.67–6825	nonstoich. spinel	Zeidler et al. (2011)
45	$Mg_{0.53}Al_{2.31}O_4$	1.67–6825	nonstoich. spinel	Zeidler et al. (2011)
46	$Mg_{0.43}Al_{2.38}O_4$	2–10000	nonstoich. spinel	Zeidler et al. (2011)
47	$CaAl_{12}O_{19}$	2–10000	hibonite	Mutschke et al. (2002)
48	TiO_2 (1)	2–5843	anatase	Posch et al. (2003), Zeidler et al. (2011)
49	TiO_2 (2)	2–5843	brookite	Posch et al. (2003), Zeidler et al. (2011)
50	TiO_2 (3)	0.47–36	rutile	Posch et al. (2003), Zeidler et al. (2011)
51	$CaTiO_4$	2–5820	perovskite	Posch et al. (2003), Zeidler et al. (2011)
52	$Mg_{0.6}Fe_{0.4}O$	0.2–500		Henning et al.(1995)
53	$Mg_{0.1}Fe_{0.9}O$	0.2–500		Henning et al.(1995)
54	FeO	0.2–500		Henning et al.(1995)
55	Fe_3O_4	0.1–100000		Kozasa
Sulfides				
56	$Mg_{0.9}Fe_{0.1}S$	10–500		Begemann et al.(1994)
57	$Mg_{0.1}Fe_{0.9}S$	10–500		Begemann et al.(1994)
58	FeS	0.1–100000		Kozasa
59	SiS_2	13–60		Begemann et al.(1996)

Table 3. Best 2-Composition Fits of Cas A Dust

Spectrum	Compositions[1]	Total Dust Mass ($M_\odot$)[2]
Ar II	$\mathbf{Mg_{0.7}SiO_{2.7}}$ + graphite, ac, FeS, C glass, Fe, be, Al_2O_3, nonstoichiomentric spinel, Fe_3O_4	0.01 ± 0.002
Ar III	$\mathbf{Mg_{0.7}SiO_{2.7}}$ + nonstoich. spinel, ac, Al_2O_3, C glass, Fe, be, graphite, hibonite, Fe_3O_4	0.004 ± 0.001
Ne II	$\mathbf{Al_2O_3}$ + be, ac, C glass, Fe, graphite, FeS, Fe_3O_4, $Mg_{0.1}Fe_{0.9}S$ (**nonstoich. spinel** + be, C glass, Fe)	0.004 ± 0.001
X-ray Fe	$\mathbf{Mg_{2.4}SiO_{4.4}}$ + be, C glass, Fe, $Mg_{0.1}Fe_{0.9}S$, ac, graphite, FeS, Fe_3O_4 $\mathbf{MgFeSiO_4}$ + be, C glass, Fe, $Mg_{0.1}Fe_{0.9}S$, ac (**other silicates** + usual “featureless” components)	0.02 ± 0.01
South Spot	$\mathbf{MgFeSiO_4}$ + C glass, ac, be, Fe $\mathbf{Mg_{2.4}SiO_{4.4}}$ + ac, Fe, be, C glass (**other silicates** + usual “featureless” components)	$0.0001 \pm 3 \times 10^{-5}$
Radio	$\mathbf{Mg_{2.4}SiO_{4.4}}$ + graphite, nonstoich. spinel, $Mg_{0.1}Fe_{0.9}S$, C glass, PAH^+, Al_2O_3, FeS, Fe, be $\mathbf{MgFeSiO_4}$ + graphite, C glass, Al_2O_3, Fe, be, FeS, $Mg_{0.1}Fe_{0.9}S$ ($\mathbf{Mg_2SiO_4}$ + C glass, Al_2O_3, graphite, Fe, be)	0.0004 ± 0.0004
Si II	Indeterminate	$\lesssim 0.1$?

[1] The compositions in **bold** need to be paired with any of the (generally) more featureless components listed after the “+” sign. These components are listed in order of increasing χ^2, but the differences are not significant. Combinations listed in parentheses have χ^2 values larger than other combinations, but still within a factor of 2 of the minimum χ^2.

[2] Mean and σ for good models in which the bold components at left are the dominant mass.

Table 4. Possible Compositions for the 12 μm Peak of Ar II, Ar III Dust

Compositions	Comment
SiO_2	requires CDE calculation of κ_λ, also contributes to 9 and 21 μm features
SiC	requires CDE calculation of κ_λ
$Mg_xAl_yO_4$ or $CaAl_{12}O_{19}$	requires extremely high temperatures [$y = (8 - 2x)/3$]